TU Delft Delft University of Technology

Witteveen + Bos

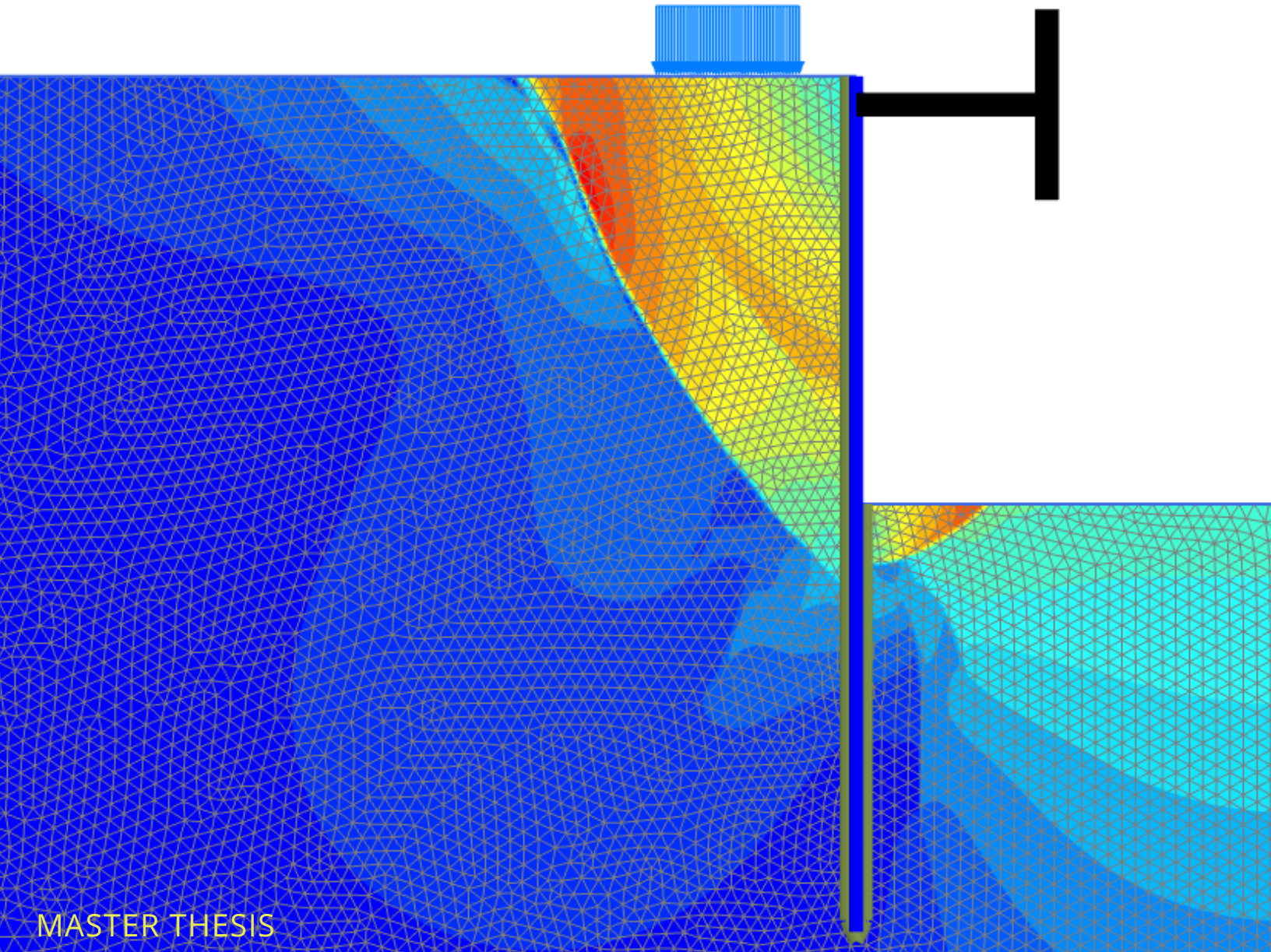

MASTER THESIS

S.R. Dhauri

EVALUATING DILATION AND MESH DEPENDENCY IN GEOTECHNICAL FEM SIMULATIONS USING NON-ASSOCIATED PLASTICITY

Evaluating Dilation and Mesh Dependency in Geotechnical FEM Simulations using Non-Associated Plasticity

MSc Thesis

by,

Sha'ief Dhauri

Assessment Committee:

Dr.ir. R.B.J. Brinkgreve - TU Delft

Dr.ir. C. Zwanenburg - TU Delft

Dr. M. Lesueur - TU Delft

Company Supervisors:

ir. A.M. Dortland - Witteveen+Bos

ir. J. de Greef - Witteveen+Bos

In partial fulfillment of the requirements for the degree of Master of Science in Civil Engineering specializing in Geotechnical Engineering at the Delft University of Technology

July 2025

TU Delft Delft University of Technology

Witteveen + Bos

Abstract

This research investigates the assumptions and limitations in geotechnical modeling, specifically focusing on the influence of using associated and non-associated flow rules in Finite Element Method (FEM) calculations. These models are used with various assumptions, including plane-strain conditions, the Mohr-Coulomb failure criterion, strength parameter determination (e.g., triaxial tests or Cone Penetration Test (CPT) correlations), (non-)associated flow rules, drained or undrained conditions, and mesh size in FEM analyses. While these assumptions simplify complex soil behavior, they can also lead to inaccuracies, making it necessary to critically assess their effects on model outcomes.

A key aspect of this research is evaluating the influence of the dilatancy angle ψ in non-associated plasticity models. In this research this influence of the dilatancy angle will mainly be assessed in a linear-elastic perfectly-plastic Mohr-Coulomb model. An associated flow rule makes the assumption that the plastic potential function g is equal to the yield function f, meaning the friction angle ϕ and dilatancy angle ψ are equal upon failure ($\psi = \phi$). However, this assumption overpredicts soil strength and can lead to unrealistic, overly optimistic designs by inaccurately modeling plastic volumetric strain. In non-associated flow rules the plastic potential function g is defined separate from the yield function f, allowing for $\psi \neq \phi$. While this assumption allows for a more accurate representation of soil behavior, it will lead to non-unique solutions. This study will assess to what extent this dilatancy angle influences model outcomes using non-associated plasticity in relation to confined and constrained deformation.

Another focus of this research is the effect of mesh refinement in FEM simulations of geotechnical structures. When using non-associated plasticity, failure can lead to strain localization, resulting in a non-unique solution that is dependent on mesh size. In practice, the degree of mesh refinement required for reliable results is not well defined. This study will investigate the level of mesh refinement necessary to ensure numerical convergence in two types of geotechnical problems: slope stability analysis of an embankment, where the goal is to achieve a stable Factor of Safety (FoS), and the bending moment along a retaining structure, where the mesh influence on results will be evaluated. The findings will contribute to proposing general or project-specific guidelines for selecting an appropriate mesh size in FEM models.

Finally, this research will assess the performance of an equivalent associated plasticity model, which provides a theoretical approach to define associated material parameters based on non-associated material parameters. While this method has been proposed as a means to improve the accuracy of non-associated flow models, its practical implementation and effectiveness in boundary value problems solved in finite element method (FEM) remain unclear. This study will evaluate the conditions under which equivalent associated plasticity can be applied in FEM calculations.

By addressing these key aspects this research aims to enhance the understanding of model assumptions and limitations in geotechnical engineering in the context of non-associated plasticity. The ultimate objective is to bridge the gap between theoretical models and real-world geotechnical applications.

Acknowledgments

First and foremost, I would like to express my gratitude to my university supervisors, Dr.ir. R.B.J. Brinkgreve, Dr.ir. C. Zwanenburg and Dr. M. Lesueur, for their guidance, expertise and critical feedback throughout the course of the research. Through their useful guidance I was able to have a solid foundation on how to start this research and what to be mindful for. They challenged me to think critically throughout the process, which allowed me to get the most out of this research.

Special thanks go to my company supervisors at Witteveen+Bos, ir. A.M. Dortland and ir. J. de Greef, for providing the topic of this research. I also would like to thank them for giving me a nice work environment for conducting my final research project. During the entire project they were actively engaged with the research, which I really appreciated. Their guidance and perspective helped me to finish this research successfully. I also appreciate the light-hearted conversations and encouraging words from the remaining colleagues at the company.

To my friends at TU Delft, thank you for the moral support and motivation. I appreciate the warm friendships I made throughout my studies in Delft and hope these will be long lasting. Our coffee breaks, drinks and diners made it a fun ride.

Finally, I would like to thank my loving family, girlfriend and friends for their support and encouragement during my academic journey. Their belief in my abilities allowed me to overcome difficult times and to finish my education.

List of symbols

ϕ	Angle of internal friction
ϕ_{cv}	Angle of internal friction at constant volume
ϕ_{mob}	Mobilized angle of internal friction
ϕ_{EQV}	Angle of internal friction for equivalent associated plasticity
ϕ_{RED}	Angle of internal friction for reduced associated plasticity
ψ	Angle of dilation
c	Cohesion
γ_{sat}	saturated unit weight
γ_{unsat}	unsaturated unit weight
β	Orientation of a shear band
α	Slope inclination of an embankment
τ	Shear stress
$\sigma_{xx}, \sigma_{yy}, \sigma_{zz}$	Cartesian normal stress
$\sigma_1, \sigma_2, \sigma_3$	Principal normal stress
$\varepsilon_1, \varepsilon_2, \varepsilon_3$	Principal strain
$\dot{\varepsilon}_1, \dot{\varepsilon}_2, \dot{\varepsilon}_3$	Rate of total principal strain
$\dot{\varepsilon}_1^e, \dot{\varepsilon}_2^e, \dot{\varepsilon}_3^e$	Rate of elastic principal strain
$\dot{\varepsilon}_1^p, \dot{\varepsilon}_2^p, \dot{\varepsilon}_3^p$	Rate of plastic principal strain
λ	Plastic (non-negative) multiplier
$\dot{\gamma}^p$	Rate of plastic distortion
θ	Lode angle
Λ	Degree of non-associativity
p	Isotropic stress
q	Deviatoric stress
f	Yield function
g	Plastic potential function
ν	Poisson's ratio
E	Young's modulus
EA	Axial stiffness
EI	Bending stiffness
R	Shear stress ratio
K_0	Earth pressure coefficient
FEM	Finite Element Method
FoS	Factor of Safety
LEM	Limit Equilibrium Method

Contents

Abstract i

Acknowledgments ii

List of symbols iii

1 Introduction 1
- 1.1 Problem description . . . 1
- 1.2 Research objective . . . 2
- 1.3 Research scope . . . 2
- 1.4 Research methodology . . . 3
- 1.5 Report structure . . . 3

2 Literature review 4
- 2.1 Non-associated plasticity . . . 4
- 2.2 The role of dilatancy angle . . . 5
- 2.3 Shear band orientation . . . 7
- 2.4 Limitations . . . 11
- 2.5 Equivalent associated plasticity . . . 11

3 Influence dilatancy angle 12
- 3.1 DSS test simulation . . . 12
- 3.2 Slope stability . . . 18
- 3.3 Retaining structure . . . 22

4 Mesh dependency 30
- 4.1 Slope stability . . . 30
- 4.2 Retaining structure . . . 33

5 Equivalent associated plasticity 38
- 5.1 DSS test simulation . . . 38
- 5.2 Slope stability . . . 40
- 5.3 Retaining structure . . . 43

6 Conclusions & recommendations 47
- 6.1 Conclusions . . . 47
- 6.2 Recommendations . . . 48

References 50

1 Introduction

In geotechnical engineering, models are essential tools used to estimate how soil and structural systems will behave under specific conditions. These models rely on a range of simplifying assumptions, such as plane strain conditions, the Mohr-Coulomb failure criterion, the application of strength parameters from triaxial to plane strain conditions, associated or non-associated flow rules, drained or undrained behavior, and mesh discretization FEM analyses. While these assumptions are necessary to make complex problems workable, they also introduce uncertainty and potential deviation from real-world behavior. Engineers must maintain a careful balance between the assumptions they make and the specific problem in hand. This principal was emphasized by Vaughan (1994), following similar views expressed by Terzaghi and Peck (1948), who also highlighted the importance of testing theory against practice. In order to make a more critical assessment of existing and new geotechnical structures, it is necessary to challenge the assumptions on which these models are based. The effect of the assumptions and approaches used by geotechnical engineers should be validated and tested to narrow the gap between models and reality. It is important to be aware of the application and limitations of assumptions and approaches used to model geotechnical problems. In particular, awareness of how specific modeling choices influence model outcomes, whether they lead to overly conservative or overly optimistic design, is crucial in geotechnical practice. This research aims to provide insight into the role and limitations of one such modeling choice: the assumption of associated versus non-associated plasticity. Through a series of simulations involving direct simple shear tests, slope stability problems, and retaining structures, this work investigates how these assumptions affect the mechanical response of soils in FEM simulations. The objective is to evaluate when and how associated or non-associated flow rules introduce biases in strength prediction, deformation, or failure mechanisms. The remainder of this chapter outlines the problem description, research objectives, and the boundaries and scope of the project.

1.1 Problem description

An associated flow rule makes the assumption that the plastic potential function g, which governs the development of plastic strain rates, is equal to the yield function f. In the literature this assumption is referred to as Drucker's Postulate (Drucker, 1959). In the context of the Mohr-Coulomb failure criterion this associated flow rule leads to the assumption that the friction angle ϕ and the dilatancy angle ψ are equal at failure ($\phi = \psi$). However, this results in an significant overestimation of soil strength and overly optimistic designs due to the incorrect prediction of plastic volumetric strain. In contrast, for the non-associated flow rule the plastic potential function g is defined separate from the yield function f, thereby the Drucker's Postulate no longer holds (Drucker, 1959). In this formulation, the dilatancy angle ψ plays a crucial role when using a non-associated flow rule, where it is independent of the friction angle ($\phi \neq \psi$). In this approach, ψ governs the relationship between plastic volumetric strain and distortion, providing a more accurate representation of granular material behavior (de Borst et al., 2022). In this context, the goal of the research will be to systematically investigate to what extent the dilatancy angle influences model outcomes using both associated and non-associated plasticity in FEM simulations

Calculating with non-associated plasticity can lead to localization upon failure and thus to a non-unique solution. When using non-softening material models, convergence to a fixed solution upon mesh refinement is not always guaranteed and must be evaluated carefully. According to the Projectoverstijgende Verkenning Macrostabiliteit guideline (POVM, 2020), local mesh refinement is required in regions where large gradients in stress or deformation are anticipated, such as near potential failure planes in slope stability analyses. To ensure numerical reliability, it must be demonstrated that further mesh refinement does not significantly alter the model outcome. However, in engineering practice excessively fine meshes often lead to very long computation time, which is impractical for routine design. Therefore, this study aims to investigate the influence of mesh refinement on model results and to identify a level of mesh fineness beyond which additional refinement has negligible effect. This will enable the formulation of practical recommendations for mesh discretization, either as a general guideline or adapted to project-specific requirements.

Davis (1968) proposed a method to relate the mobilized shear strength in a slip plane in non-associated materials to an equivalent associated formulation. This approach establishes a theoretical link between associated and non-associated plasticity by adjusting the friction angle such that calculations using an associated flow rule can replicate the strength behavior of non-associated materials. In essence, it enables the use of numerically more stable associated plasticity while preserving realistic strength predictions. This research aims to evaluate the applicability of this equivalent associated plasticity approach in FEM simulations and to determine its performance across different geotechnical applications.

1.2 Research objective

The aim of the research is to provide insight on assumptions and limitations in geotechnical models concerning associated and non-associated plasticity, and to investigate how they influence the model outcome in terms of theoretical optimism or conservatism in relation to different applications. The primary goal is to understand how to ultimately obtain a realistic outcome or have an idea on degree of optimism or conservatism introduced by modeling assumptions. The research will focus on the influence of using an associated and non-associated flow rule and the role of the dilatancy ψ and friction angle ϕ in relation to confined and constrained deformation. Additionally, the mesh dependence in FEM models using associated and non-associated plasticity will be discussed. The aim will be to provide clarification in which level of mesh refinement is refined enough for standard engineering practice for typical geotechnical problems. Two boundary value problems will be investigated in this context: (1) slope stability (2) a retaining structure. The hypotheses is that the dilatancy angle ψ will play a more significant role with increased restriction in confined and constrained deformation. Finally, the applicability of equivalent associated plasticity, based on approaches such as that proposed by Davis (1968), will be explored. This includes assessing the conditions under which this method can be applied effectively in FEM simulations. In this context, the following research questions are formulated:

- **RQ1:** What is the influence of the dilatancy angle ψ, in relation to confined and constrained deformation, in the case of associated and non-associated plasticity?
- **RQ2:** Which level of mesh refinement converges the model outcome of a slope stability and retaining structure problem when using non-associated plasticity in FEM?
- **RQ3:** Under which conditions can equivalent associated plasticity be applied in FEM models?

1.3 Research scope

The research will challenge assumptions and highlight limitations in geotechnical modeling practices. The primary focus will be on the role of dilatancy angle ψ in associated and non-associated plasticity in relation to confined and constrained deformation. Given the significance of the dilatancy angle, the research will mainly include drained dense sands, as these materials have the most relevant mechanical properties for this research. For the research the various alternatives of the Mohr-Coulomb failure criterion (e.g. Matsuoka-Nakai or Lade) will not be taken into account to show their influence on strength. How the equivalent associated plasticity can be applied in FEM and how it performs will also be highlighted. Topics such as parameter determination from laboratory testing and undrained behavior are beyond the scope of this study and will not be addressed.

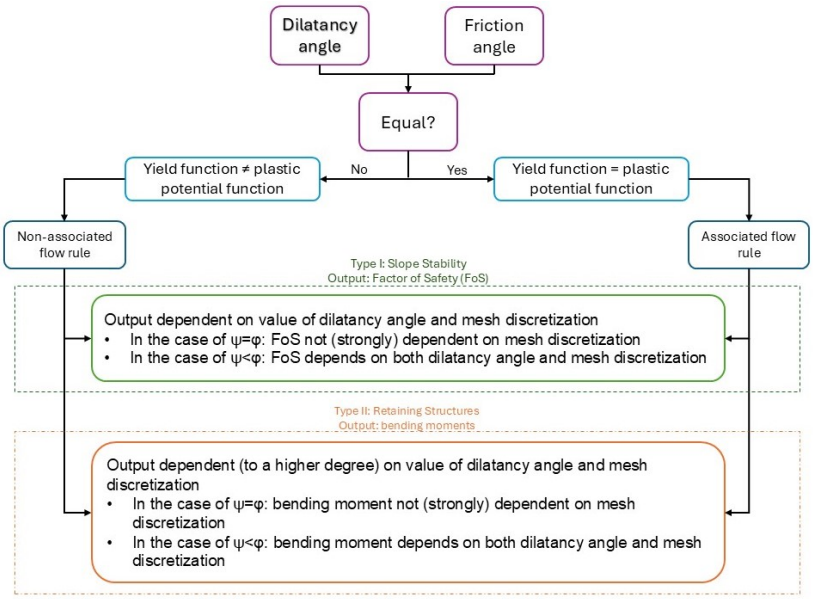

Figure 1: Conceptual framework

1.4 Research methodology

The research will be carried out in four main phases, each contributing to a systematic approach in answering the research questions: literature review, numerical modeling, testing & validation and analysis & recommendation. In the literature review phase extensive research on the relevant theories and assumptions is carried out, with a particular focus on associated and non-associated plasticity, dilatancy, and mesh dependency in FEM. In the numerical modeling phase, the theoretical insights from the literature will be applied to two representative boundary value problems. The first involves a slope stability analysis of an embankment, with the factor of safety (FoS) as model outcome. The second involves a retaining structure, where the focus will be on evaluating the convergence behavior of bending moments. The conceptual framework of this study is illustrated in Figure 1

1.5 Report structure

The following chapter discusses the theoretical framework supporting the research. This includes an in depth review of associated and non-associated plasticity, the role of the dilatancy angle ψ, shear band orientation, limitations and opportunities of current models, and the concept of equivalent associated plasticity. Relevant studies and key equations are evaluated to establish the basis for the numerical analyses.

Chapter 3 focuses on the role of the dilatancy angle ψ in both associated and non-associated plasticity framework. This chapter demonstrated the influence of ψ through numerical simulations, including DSS tests, a slope stability problem and retaining structure problem. The numerical simulations are used to assess how ψ influences strength and plastic deformation under varying levels of confined and constrained deformation.

Chapter 4 investigates the sensitivity of FEM model outcome to mesh refinement for both associated and non-associated plasticity. The mesh dependence is studies for two geotechnical problems: a slope stability analysis and a retaining structure model. This chapter provides recommendations on mesh refinement levels required for reliable results.

Chapter 5 the applicability of equivalent associated plasticity to mitigate numerical issues inherent in non-associated flow rules while maintaining modeling accuracy. This chapter includes validation through DSS test simulations and assessment of the potential of this method through a slope stability analyses and retaining structure model.

Chapter 6 provides a summary of the findings of the research, answering the formulated research questions, and provides recommendations for engineering practice in the field of geotechnical FEM modeling.

2 Literature review

This chapter provides the theoretical foundation for th research by reviewing key concepts related to soil plasticity and numerical simulations. It introduces the principles of associated and non-associated plasticity, emphasizing the importance of the dilatancy angle ψ in capturing realistic soil behavior. The Mohr-Coulomb failure criterion and it variation are discussed, along with their limitations and opportunities in geotechnical models. Furthermore, the chapter addresses the issue of mesh dependency in FEM simulations and introduces the concept of equivalent associated plasticity as a means to balance accuracy and numerical stability.

2.1 Non-associated plasticity

General analytical approaches for designing geotechnical structures make the assumption of an associated flow rule, meaning the friction angle (ϕ) and the dilatancy angle (ψ) are equal upon failure ($\phi = \psi$). This assumption tends to overpredict the strength of the soil, leading to a too optimistic design. The root of the problem lies in the incorrect prediction of the plastic volumetric flow in granular materials with the use of an associated flow rule. This incorrect prediction of the plastic volumetric strain will be compensated by elastic volumetric strain in kinematically constrained conditions, leading to much higher stresses than occur in reality (de Borst et al., 2022). Figure 2 illustrates this overprediction by comparing the actual measured volumetric strain in a triaxial test and the volumetric strain predicted with an associated flow rule for a Mohr-Coulomb yield criterion.

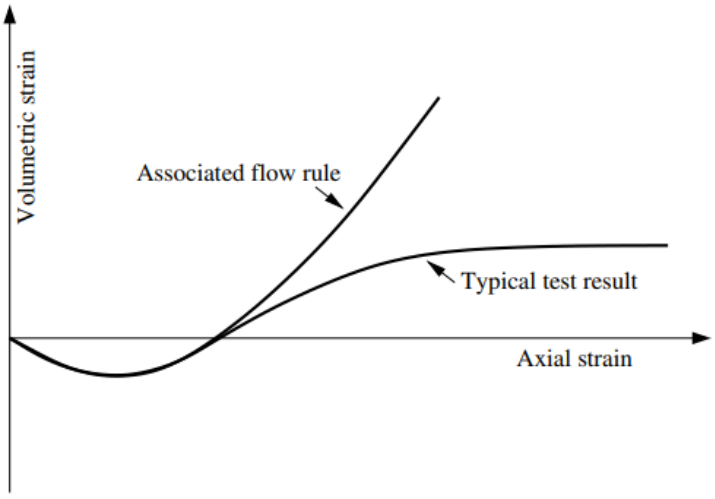

Figure 2: Typical result of a triaxial test on a granular material, in which the volumetric strain is plotted as a function of the axial strain together with the volume increase that would be generated by an associated flow rule (de Borst et al., 2022)

An alternative for this assumption is an non-associated flow rule, which assumes the friction angle (ϕ) to be different from the dilatancy angle (ψ) upon failure ($\phi \neq \psi$). The non-associated flow rules incorporate a plastic potential function, independent of the yield function, in which the plastic rates are derived by differentiation with respect to the stress tensor. Equation 1 gives a yield function f based on the Mohr-Coulomb failure criterion, with σ_1 being the major principal stress and σ_3 the minor principal stress (de Borst et al., 2022). Its important to note that this holds in absolute sense. The stresses in the Mohr-Coulomb circle represent compression stresses. As soil cannot hold tensile stresses, these compression stresses are often taken as positive. In reality the dilatancy angle will be much smaller than the friction angle. For quartz sand the dilatancy angle will typically be $\psi \simeq \phi - 30°$ (Vermeer, 1990).

$$f = \frac{1}{2}(\sigma_1 - \sigma_3) + \frac{1}{2}(\sigma_1 + \sigma_3)\sin\phi - c\cos\phi \tag{1}$$

Equation 2 represents the plastic potential function g,in terms of principal stresses, incorporated by the non-associated flow rule. The only difference from the Mohr-Coulomb yield function f and the plastic potential

function g is the replacement of the friction angle ϕ with the dilatancy angle ψ (Vermeer and de Borst, 1984).

$$g = \frac{1}{2}(\sigma_1 - \sigma_3) + \frac{1}{2}(\sigma_1 + \sigma_3)\sin\psi - c\cos\psi \tag{2}$$

Differentiating Equation 2 with respect to the principal stress Equation 3 is obtained, which represents the plastic strain rates or the flow rule (Vermeer and de Borst, 1984).

$$\begin{bmatrix} \dot{\varepsilon}_1^p \\ \dot{\varepsilon}_2^p \\ \dot{\varepsilon}_3^p \end{bmatrix} = \lambda \begin{bmatrix} \frac{\partial g}{\partial \sigma_1} \\ \frac{\partial g}{\partial \sigma_2} \\ \frac{\partial g}{\partial \sigma_3} \end{bmatrix} = \lambda \begin{bmatrix} \frac{1}{2} + \frac{1}{2}\sin\psi \\ 0 \\ -\frac{1}{2} + \frac{1}{2}\sin\psi \end{bmatrix} \tag{3}$$

In numerical analyses it is this flow rule, rather than the plastic potential function g itself, that is implemented in the actual computation (Vermeer and de Borst, 1984). Equation 3 shows that the dilatancy angle ψ plays an important part in a non-associated flow rule. In this context, the research will go into the influence of this dilatancy angle, in relation to confined and constrained deformation, in the case of non-associated plasticity.

2.2 The role of dilatancy angle

An important difference in non-associated plasticity theory is the inclusion of the dilatancy angle ψ, which governs the inelastic (plastic) volume changes. Dilation may be described as the change in volume due to shear distortion. A suitable parameter to characterize the degree of dilatancy in materials is the dilatancy angle. Through tests it has been shown that the dilatancy angle is typically significantly lower than the friction angle for soils (Vermeer and de Borst, 1984). In the literature the difference between the friction angle and the dilatancy angle of soil is referred to the degree of non-associativity Λ. The degree of non-associativity is determined through Equation 4.

$$\Lambda = \phi - \psi \tag{4}$$

The significance of the dilatancy angle ψ can be shown through a simple shear test on a dense sand. In a typical shear stress - shear strain relation (Figure 3a) usually a peak will be observed, followed by a reduction in shear strength upon further loading. Therefore a distinction is made between the peak and large strain (residual) friction angles, denoted as ϕ_p and ϕ_{cv} respectively. The subscript "cv" denotes that shearing takes place at "constant volume", meaning that no dilation occurs. In a simple shear test, illustrated in Figure 3c, a dense sand expands in volume, referred to as dilation. This usually takes place after a small initial compaction, as illustrated in Figure 3b. The magnitude of this expansion strongly depends on the density of the sample, as denser soils will expand more rapidly (Houlsby, 1991).

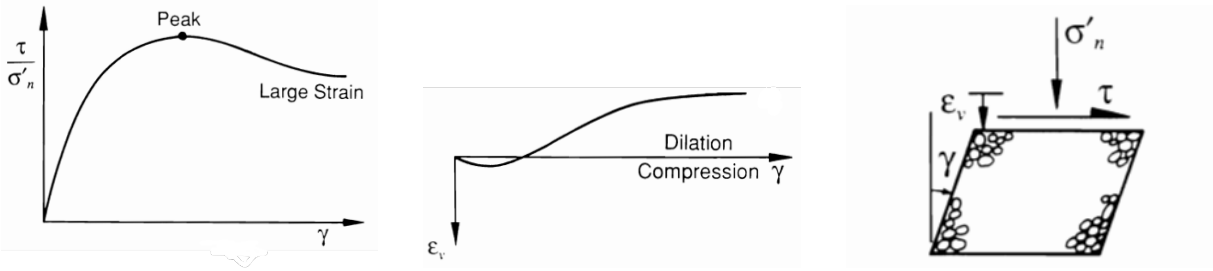

(a) (b) (c)

Figure 3: Typical curves of a simple shear test on a dense sand (a) shear stress - shear strain relation (b) volumetric strain - shear strain relation (c) geometry, stress and strains Houlsby (1991)

In Figure 4 the Mohr's circles for stress and strain rate are illustrated for a cohesionless ($c = 0$) soil. As Figure 4a illustrates, the friction angle ϕ can be expressed as the ratio between the shear stress to the normal stress. This expression can be defined in terms of principal stresses (Houlsby, 1991):

$$\sin\phi = \frac{\sigma_1 - \sigma_3}{\sigma_1 + \sigma_3} \tag{5}$$

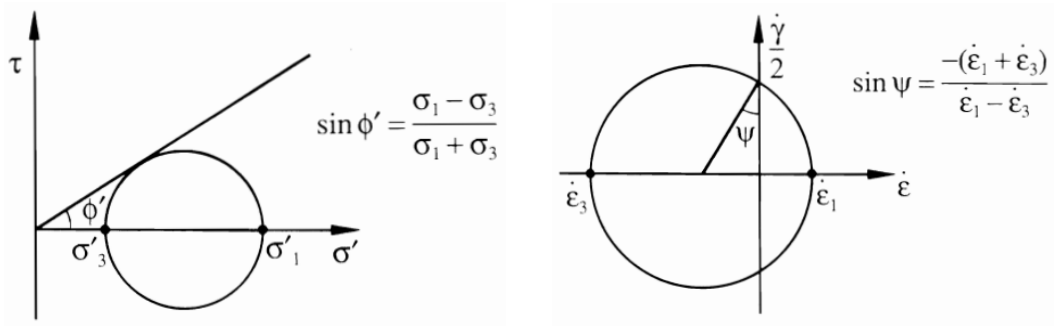

(a) (b)

Figure 4: Mohr's circle for (a) stress and (b) strain rate (Houlsby, 1991)

In a similar manner Figure 4b the dilatancy angle ψ can be expressed as the ratio between the volumetric strain rate and the shear strain rate. In the case of plain strain ($\varepsilon_2 = 0$) in terms of principal strain rates can be defined as (Houlsby, 1991):

$$\sin\psi = -\frac{\dot{\varepsilon}_1 + \dot{\varepsilon}_3}{\dot{\varepsilon}_1 - \dot{\varepsilon}_3} \tag{6}$$

In defining the dilatancy angle ψ it is important to distinguish between elastic (reversible) strain and plastic (irreversible) strain. The dilatancy angle ψ should be strictly defined in terms of plastic components of the strain rates (Houlsby, 1991).

$$\varepsilon = \varepsilon^e + \varepsilon^p \tag{7}$$

With this the definition of the dilatancy angle ψ can be modified to (Roscoe, 1970; Houlsby, 1991):

$$\sin\psi = -\frac{\dot{\varepsilon}_1^p + \dot{\varepsilon}_3^p}{\dot{\varepsilon}_1^p - \dot{\varepsilon}_3^p} \tag{8}$$

In theory it would mean that determining the dilatancy angle ψ from a test becomes more difficult, as a distinction should be made between the elastic and plastic components of the shear strain. In practice this distinction appears to be irrelevant as, for most soils, the elastic stiffness is sufficiently high such that the elastic strains are significantly smaller than the plastic strains. In particular, at the peak in several commonly used shear tests the stress remains unchanged, resulting in zero elastic strain rates (Houlsby, 1991). One could also argue that during plastic deformation stress will remain roughly constant resulting in trivial elastic strain, as change in stress is directly related to elastic strain. This means that in practice Equations 6 and 7 coincide.

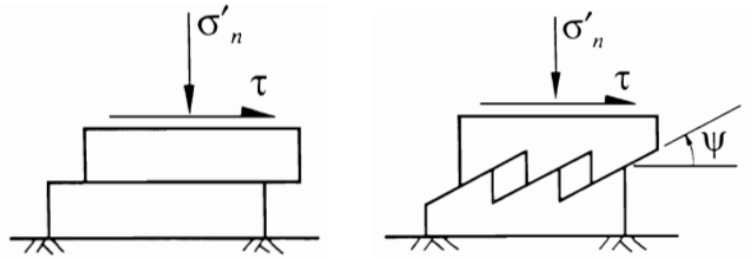

(a) (b)

Figure 5: The sawtooth model for (a) the case of $\psi = 0°$ (b) the case of $\psi \neq 0°$ (Houlsby, 1991)

In Figure 5 the relation between the friction angle and the dilatancy angle is illustrated using the sawtooth model. The case of $\psi = 0°$ is illustrated by a frictional block sliding over another on a flat plane (Figure 5a). The friction angle in this case is represented by the constant volume friction angle ϕ_{cv} where that shearing takes place at constant volume, which means that no dilation occurs (Houlsby, 1991). The ratio between the shear stress and normal stress is in this case defined by:

$$\frac{\tau}{\sigma_n} = \tan \phi_{cv} \tag{9}$$

The case of $\psi \neq 0°$ is illustrated by a sawtooth with teeth inclined at an angle ψ and the same friction angle ϕ_{cv} acting on these teeth. The friction angle ϕ is now the sum of the constant volume friction angle ϕ_{cv} and the dilatancy angle ψ. This relationship is referred to as the flow rule (Houlsby, 1991). The ratio between the shear stress and normal stress now becomes:

$$\frac{\tau}{\sigma_n} = \tan \phi = \tan(\phi_{cv} + \psi) \tag{10}$$

In the literature more sophisticated models exist to define the relation between the constant volume friction angle and the dilatancy angle. Bolton (1986) defined this relation based on a purely empirical approach. This relation is defined as Equation 11.

$$\phi = \phi_{cv} + 0.8\psi \tag{11}$$

It is important to note that the dilatancy angle plays a significant role as it influences the appropriate friction angle. In confined and constrained soil conditions the effect of dilation is more pronounced. As soil becomes increasingly constraint, its ability to deform is limited, and the effects of dilation are more pronounced. In less confined soil conditions like slopes, soil can deform freely, the role of dilation is much less important except for its effect on strength (Houlsby, 1991).

Apart from the strength of a soil, the dilatancy angle also defines the plastic strain generated. This phenomenon is illustrated in Figure 6. In this Figure a stress path in the case of $\psi = 0°$ and the case of $\psi = \phi$ is illustrated in the deviatoric plane (Figure 6a) and in principal stress space (Figure 6b). In Figure 6a two Mohr-Coulomb contour cross-sections are shown for the two different cases of $\psi = 0°$ and $\psi = \phi$. The stress paths for these two cases coincide until failure. In the case of $\psi = 0°$ failure was reached at a principal stress of $p = 85.82\ kPa$ and in the case of $\psi = \phi$ failure was reached at $p = 146.25\ kPa$.

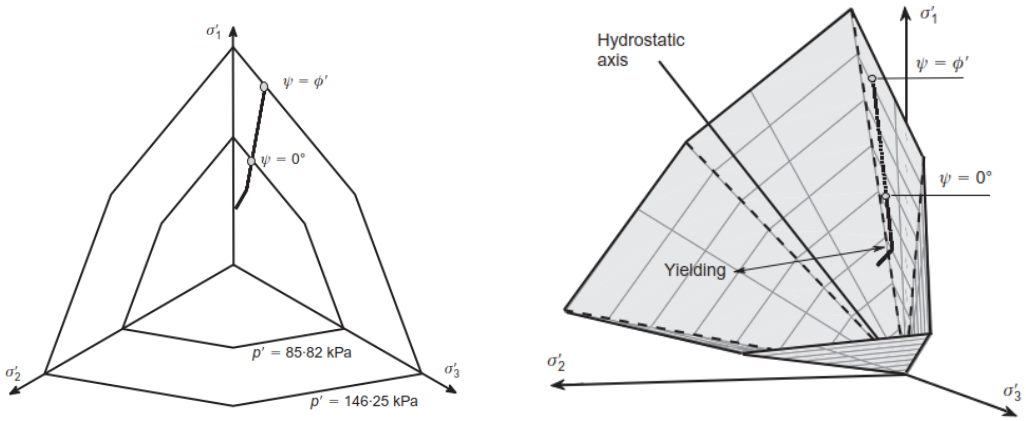

Figure 6: Stress paths concerning a simple shear test for $\psi = \phi$ and $\psi = 0$ in (a) the deviatoric plane (b) three-dimensional view in the principal stress space (Di Prisco and Pisanò, 2011)

From Figure 6 it can be observed that the case of $\psi = \phi$ shows more plastic deformation, compared to the case of $\psi = 0°$. This falls in line with the statement that the dilatancy angle ψ governs the plastic deformation, with a more dilatant material showing more plastic strain.

2.3 Shear band orientation

Through numerical simulations, experiments and practical problems it has been shown that localization of deformations is one of the most frequent failure modes of soils. In frictional material, like sand, the localization will be in the form of a shear band as illustrated in Figure 7 (Teunissen, 2008).

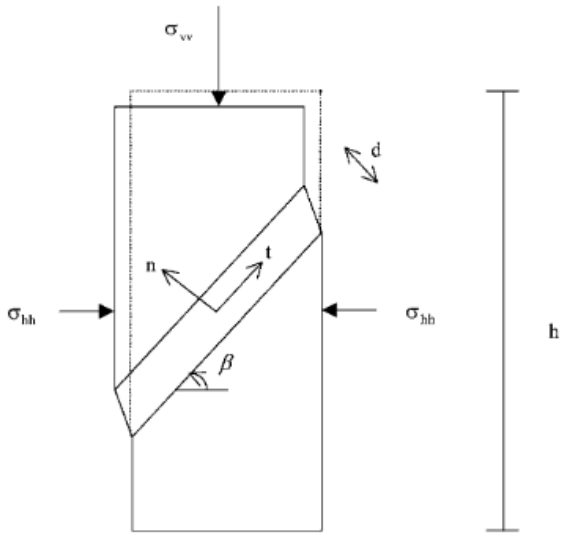

Figure 7: Geometry of biaxial test with shear band (Teunissen, 2008)

The orientation of the shear band β will be between two limits. These two limits are $\beta_{Coulomb}$ and β_{Roscoe}, which will follow Equation 12 and 13 respectively (Teunissen, 2007). The difference between these two orientations is significant, as the friction angle ϕ is usually much larger than the dilatancy angle ψ. The difference is in the range of 30°. Efforts to validate either the $\beta_{Coulomb}$ or β_{Roscoe} orientation have shown that both are supported by experimental evidence, with results varying depending on the material type and falling within a certain range. The experimental data indicates that the actual orientation of the shear bands varies between these two limits and that fine sands typically form Coulomb-type shear bands, whereas coarse sands tend to form Roscoe-type shear bands (Vermeer, 1990).

$$\beta_{Coulomb} = 45° + \frac{\phi}{2} \tag{12}$$

$$\beta_{Roscoe} = 45° + \frac{\psi}{2} \tag{13}$$

The orientation $\beta_{Coulomb}$ follows from maximum strength and the orientation β_{Roscoe} follows from maximum plasticity (Teunissen, 2022). The orientation of $\beta_{Coulomb}$ and β_{Roscoe} in the Mohr's circle is illustrated in Figure 8, where they are defined as the angle between the principal stress/strain direction and the local stress/strain direction. Mohr's circle is determined through the center of the circle $\sigma_m = (\sigma_1 + \sigma_3)/2$ and the radius of the circle $\tau_m = (\sigma_1 - \sigma_3)/2$, with σ_1 representing the major principal stress and σ_3 representing the minor principal stress. The circle hits the envelope when $\sin\phi = \tau_m/(c\cot\phi + \sigma_m)$. This can be reduced to $\tau_m c\cos\phi + \sin\phi\sigma_m$, which can be written as the yield function $f = \tau - c\cos\phi - \sin\phi\sigma_m$. In the case of $f < 0$ there will be elastic behavior and in the case of $f = 0$ there will be plastic behavior where the stresses will follow the yield criterion. Stress states in the special case of $f > 0$ will theoretically result in stresses above the yield criterion (Teunissen, 2016), highlighted by "impossible stress states" in Figure 8. The plastic strains in the Mohr-Coulomb model are determined through the plastic potential $g = \tau_m - c\cos\psi - \sin\psi\sigma_m$. As previously mentioned, ψ represent the dilatancy angle and governs the degree of plastic volume strain. The plastic strain generated are defined by the derivative of the plastic potential with respect to stress $\frac{dg}{d\sigma}$. In principal space this will lead to $d\varepsilon_1^p = d\lambda(\frac{1}{2} - \frac{1}{2}\sin\phi)$ and $d\varepsilon_3^p = d\lambda(-\frac{1}{2} - \frac{1}{2}\sin\phi)$. In these formulas $d\lambda$ represents the plastic multiplier, which is a measure of the degree of plasticity. The plastic multiplier is set in place in order to satisfy the consistency relation. This relation allows stresses to stay on in yield contour $f = 0$ in plastic behavior, even if the stress state changes (Teunissen, 2016).

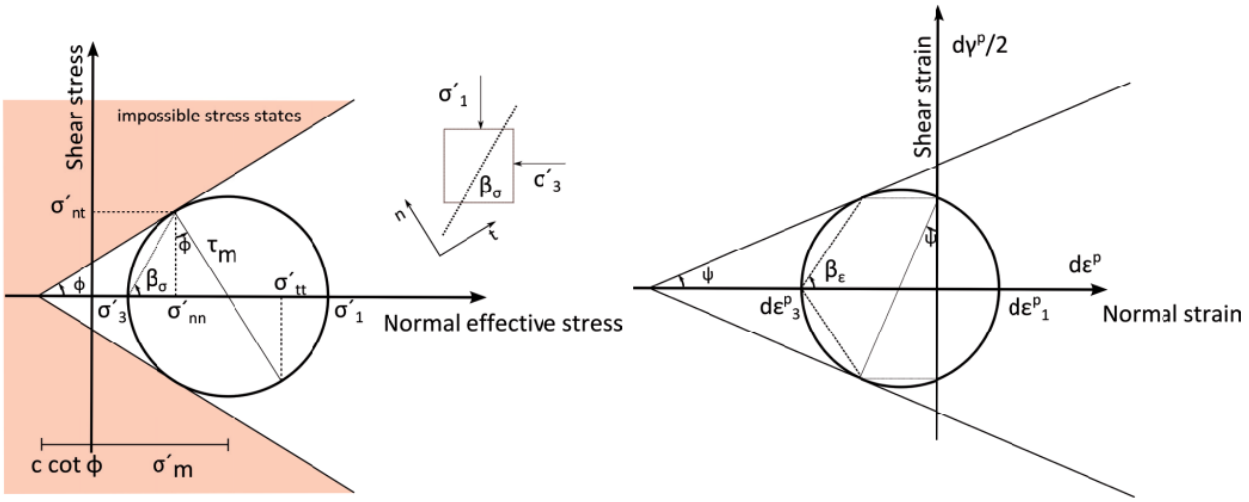

(a) (b)

Figure 8: Mohr's circle for (a) stress with $\beta_{Coulomb} = \beta_\sigma = 45° + \frac{\phi}{2}$ (b) strain with $\beta_{Roscoe} = \beta_\varepsilon = 45° + \frac{\psi}{2}$ (Teunissen, 2016)

Teunissen (2016) highlighted that the orientation of the shear band can be linked to strength. The orientation $\beta_{Coulomb}$ follows from the maximum shear strength (Equation 14), and the orientation β_{Roscoe} follows from the maximum ratio between plastic normal deformation and plastic shear deformation with respect to the minor principal stress. Only through the orientation β_{Roscoe} continuous plastic deformation is possible. The shear strength that follows from the orientation β_{Roscoe} is as represented in Equation 15 (Teunissen, 2016). Teunissen (2022) mentioned that $\beta_{Coulomb}$ follows for maximum strength and β_{Roscoe} follows for maximum plasticity. Roscoe (1970) mentioned that the orientation of the slip line must be influenced by the plastic flow rule.

$$\tau = c + \sigma \tan \phi \tag{14}$$

$$\tau = c\frac{\cos\psi\cos\phi}{1 - \sin\psi\cos\phi} + \sigma\frac{\cos\psi\sin\phi}{1 - \sin\psi\sin\phi} \tag{15}$$

Equation 15 directly follows from the Davis approach. Davis (1968) stated that only in the case of $\psi = \phi$ the classical Coulomb equation, as defined in Equation 14, is satisfied. For any other non-associated case of $\psi \neq \phi$, the strength parameters on the slip planes no longer satisfy the Coulomb equation (Equation 14). Therefore, the strength in the slip plane is defined as Equation 16 (Davis, 1968).

$$\tau_k = c_k + \sigma_k \tan \phi_k \tag{16}$$

Theoretically, Equation 16 will hold if c_k and ϕ_k are used as cohesion and friction angle in the slip planes. In the case of associated plasticity ($\psi = \phi$) c_k and ϕ_k are equal to the Coulomb c and ϕ. However, when $\psi < \phi$ both c_k and ϕ_k are less than the Coulomb c and ϕ and Equation 17 and 18 can be used to calculate their values (Davis, 1968).

$$c_k = \frac{c\cos\psi\cos\phi}{1 - \sin\psi\sin\phi} \tag{17}$$

$$\tan\phi_k = \frac{\cos\psi\sin\phi}{1 - \sin\psi\sin\phi} \tag{18}$$

Substituting c_k and ϕ_k, for the case of $\psi < \phi$, in Equation 16 will result in Equation 15, which holds for any case of $\psi < \phi$. In the special case of plastic deformation at constant volume, $\psi = 0°$, the strength parameters are defined as follows (Davis, 1968).

$$c_k = c\cos\phi \tag{19}$$

$$\tan \phi_k = \sin \phi \tag{20}$$

Substituting c_k and ϕ_k, for the case of $\psi = 0°$, in Equation 16 will result in Equation 21.

$$\tau = c \cos \phi + \sigma \sin \phi \tag{21}$$

The difference between the definitions of the upper and lower limit following the two approaches for strength, as defined in Equation 14 and 21, gets greater with an increase in friction angle. The difference in strength following the two approaches is especially noticeable with $\phi > 20°$. When a slip circle is analyzed for actual embankment failure or to validate a FEM simulation, it is essential to base the analysis on the $\sin \phi$ strength relation (Teunissen, 2016). The difference in strength is illustrated in Figure 9, in which the blue line represents the $\sin \phi$ relation (Equation 21) and the red line represents the $\tan \phi$ relation (Equation 14).

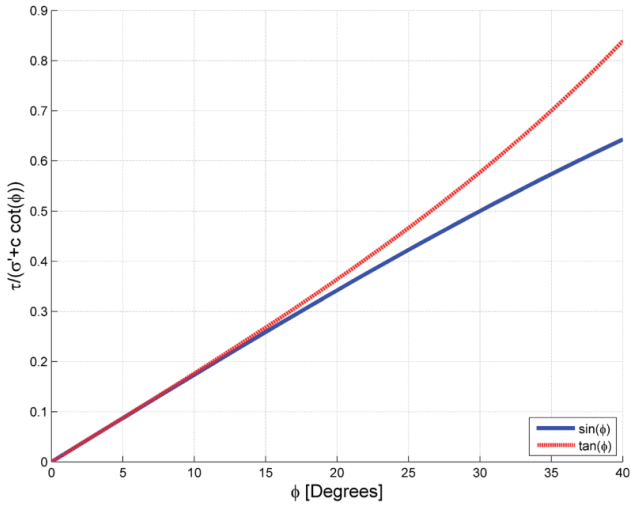

Figure 9: Upper and lower limit of shear stress ratio for a non-dilatant material with different friction angles (Teunissen, 2016)

The applied failure criteria also yields a difference in strength for a non-dilatant material. The Coulomb strength will follow the $\tan \phi$ relation as defined in Equation 14 and the Davis strength will follow the $\sin \phi$ relation as defined in Equation 21 for a non-dilatant material. The difference in strength is illustrated in Figure 10 for different friction angles.

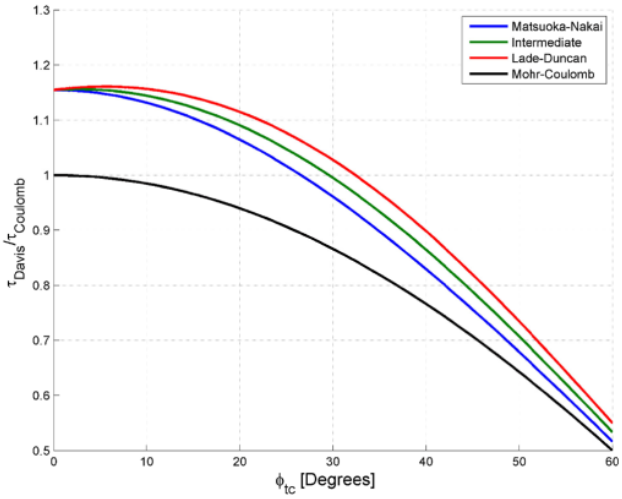

Figure 10: The Davis strength normalized to the Coulomb strength for different failure criteria for non-dilatant material with different friction angles (Teunissen, 2022)

Overall, the shear band that will form in a failure mechanism is not known upfront. It is known between which theoretical limit the orientation of the shear band will form. The actual shear band will form somewhere between these limits. In a simulation to predict a failure mode of a geotechnical structure (i.e. slope, footing, retaining structure) an assumption can be made on the expected orientation of the shear band. It is very important to justify which orientation will be assumed, as this will have a significant effect on the strength.

2.4 Limitations

In calculation models following an associated flow rule the output will not be strongly mesh dependent. However, Calculations involving non-associated plasticity can lead to localization upon failure, resulting in a non-unique and strongly mesh-dependent solution de Borst (1987); de Borst and Sabet (2019). When using non-softening models, the solution will generally converge to a fixed output with increased mesh refinement. In FEM, a slope stability problem generally a decrease of factor of safety (FoS) will be observed with a increase in mesh density (Teunissen, 2016; Tschuchnigg et al., 2015). A displacement based finite element analyses adopting a strength reduction technique will show numerical instability when imposing non-associated plasticity. This is especially the case with high friction angles and relatively low dilatancy angle (Tschuchnigg et al., 2018), meaning that an increase in degree of non-associativity Λ will lead to an increase in numerical instability and mesh dependence.

The displacement based FEM analyses in PLAXIS 2D determines a FoS of a slope by a so called ϕ/c-reduction also referred to as strength reduction. The method of strength reduction was first introduced by Zienkiewicz et al. (1975), which is achieved by gradually reducing $\tan\phi$ and c until equilibrium is no longer satisfied. This leads to the following definition of the factor of safety (Brinkgreve et al., 2016), where the "mobilized" subscript represents the strength quantities at failure:

$$FoS = \frac{\tan\phi}{\tan\phi_{mobilized}} = \frac{c}{c_{mobilized}} \tag{22}$$

In the case of associated flow rule, both the friction angle ϕ and dilatancy angle ψ will be reduced simultaneously. In the case of non-associated flow rule the friction angle ϕ is reduced and the dilatancy angle ψ is kept constant, as long as the friction angle ϕ is larger than the dilatancy angle ψ ($\phi > \psi$). The moment the friction angle ϕ is equal to the dilatancy angle ψ, both values will be reduced at the same time (Brinkgreve et al., 2016).

User-defined model reduces $\tan\phi$, $\tan\psi$ and c simultaneously. As a consequence the degree of non-associativity is also affected by the reduced ψ.

$$FoS = \frac{\tan\phi}{\tan\phi_{mobilized}} = \frac{c}{c_{mobilized}} = \frac{\tan\psi}{\tan\psi_{failure}} \tag{23}$$

2.5 Equivalent associated plasticity

As previously mentioned applying non-associated plasticity in geotechnical calculations causes discrepancies in the model outcome. Although non-associated plasticity allows to model soil behavior in a more realistic manner, this method causes instability and mesh dependency in the model outcome (Chen et al., 2019). An associated flow rule does not cause these discrepancies in numerical instability and will not show strong mesh dependence. However, in slope stability analyses an associated flow rule may overestimate the FoS of a geotechnical structure. Therefore, an equivalent associated plasticity will be assessed which allows to calculate with associated plasticity based on non-associated parameters. In this case the output of the model will not be strongly mesh dependent. The equivalent associated parameters will be determined through equation 18 as defined by Davis (1968).

3 Influence dilatancy angle

This chapter investigates the influence of the dilatancy angle ψ on model outcome when using associated ($\psi = \phi$) and non-associated plasticity ($\psi = 0°$). The analysis begins with Direct Simple Shear (DSS) test simulations to demonstrate the impact of ψ on shear strength and plastic deformation. The study then extends to practical geotechnical applications, including slope stability and retaining structure models, to illustrate how the dilatancy angle ψ plays a significant role particularly under confined and constrained conditions. The findings highlight the importance of selecting an appropriate plasticity formulation, associated or non-associated, based on the specific characteristics of the problem, particularly the boundary conditions and expected deformation modes.

3.1 DSS test simulation

To isolate and better understand the influence of the dilatancy angle ψ, this section presents a series of DSS test simulations in PLAXIS SoilTest. The DSS test provides a controlled environment for studying shear behavior under plane strain conditions with constant vertical stress, making it particularly suitable for examining the effects of plastic flow rules. By incrementally varying the dilatancy angle, from fully non-dilatant ($\psi = 0°$) to fully associated flow ($\psi = \phi$), the impact on shear strength and plastic strain development can be clearly assessed. These results serve as a conceptual foundation for interpreting the influence of ψ in more complex geotechnical problems addressed later in this chapter. For the DSS simulations, the Mohr-Coulomb constitutive model is applied and the corresponding material properties of the simulated sample are listed in Table 1. As previously mentioned, in this research the main focus will be on drained dense sands, thus the material properties are chosen accordingly.

Table 1: Material parameters used for the simulated soil sample in the DSS test

Description	Symbol	Value
Unsaturated unit weight	γ_{unsat}	0 kN/m^3
Saturated unit weight	γ_{sat}	0 kN/m^3
Young's modulus	E'_{ref}	10,000 kN/m^2
Poisson's ratio	ν	0.3
Cohesion	c'_{ref}	0 kN/m^2
Friction angle	ϕ	30°

In the DSS simulation, the unit weight of the soil sample is irrelevant and therefore set to zero. The friction angle ϕ is held constant at 30°, while the dilatancy angle ψ is varied within the range $0° < \psi < \phi$. The test conditions applied in PLAXIS SoilTest are listed in Table 2. These conditions will remain unchanged throughout the report and will be applied to every DSS simulation to ensure comparability of the results.

Table 2: Test conditions applied in the DSS simulations

Description	Value
Type of test	Drained
Initial vertical stress σ_{yy}	100 kN/m^2
Maximum shear strain	20%
Number of steps	100

The first validation of the maximum mobilized shear strength follows through a shear stress - shear strain relation from the simulated DSS test. In Figure 11a the shear stress and shear strain relation is illustrated for cases $\psi = \phi$ and $\psi = 0°$ under isotropic initial conditions ($K_0 = 1$). In the case of $\psi = \phi$, the mobilized shear strength follows the classical Coulomb equation with the $\tan\phi$ relation (Equation 14). Given an initial vertical stress of $\sigma_{yy} = 100kN/m^2$ and a friction angle of 30°, the classical Coulomb relation will yield a mobilized shear strength of $\tau = 100kN/m^2 \cdot \tan(30°) = 57.7kN/m^2$. In the case of $\psi = 0$ the mobilized shear strength follows the Davis approach for non-dilatant material with the $\sin\phi$ relation (Equation 21). Under the same test conditions the Davis approach for non-dilatant material will yield $\tau = 100kN/m^2 \cdot \sin(30°) = 50kN/m^2$. Every case of $0 < \psi < \phi$ follows the Davis approach for dilatant material as defined in Equation 15. This

is illustrated in Figure 11b. Note that the Davis approach (Equation 15) also holds for negative dilatancy angles, which simulates compaction. This means the theoretical range for ψ lies within $-\phi < \psi < \phi$. However, compaction is beyond the scope of this research and will not be further evaluated. This simulation validates that the dilatancy angle ψ governs the maximum mobilized shear strength in a slip plane, with higher dilatancy angles resulting in higher resistance.

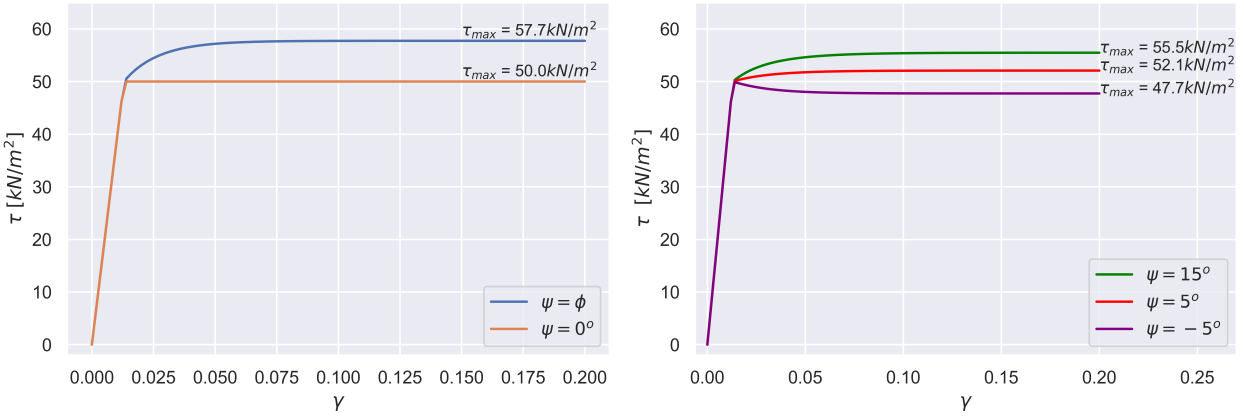

(a) (b)

Figure 11: Shear stress - shear strain relation from a DSS test simulation with $\phi = 30°$ and $K_0 = 1$ for the case of: (a) $\psi = \phi$ and $\psi = 0°$; (b) $\psi \neq \phi$

The case of $\psi = 0°$ in Figure 11a shows linearly elastic-perfectly plastic Mohr-Coulomb behavior. After yielding the stress-strain curve plateaus, indicating that the shear strength has been fully mobilized and no further stress can be sustained. This is a consequence of the material not being able to develop further plastic strain after yielding. The material will show zero plastic strain. This is validated by the stress path presented in the figure below, which confirms that no continued plastic deformation occurs once the failure envelope is reached.

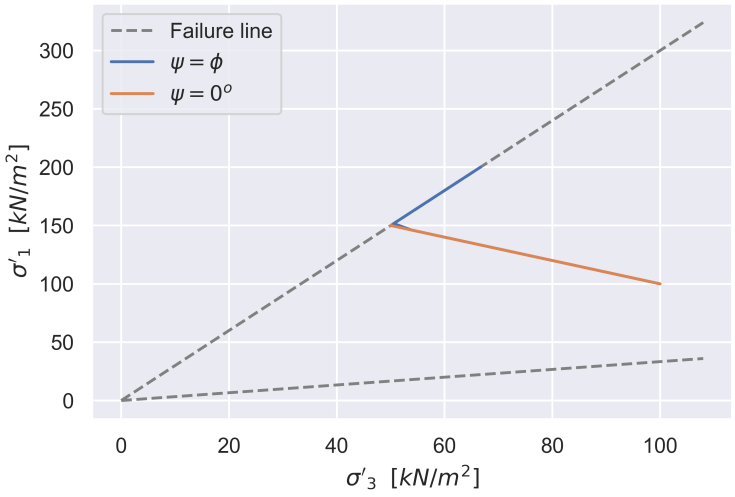

Figure 12: Stress path from a DSS test simulation with $\phi = 30°$ and $K_0 = 1$ for the case of $\psi = \phi$ and $\psi = 0°$

As can be seen in Figure 12, both cases of $\psi = \phi$ and $\psi = 0°$ start from the same initial stress state, as they share the same initial conditions. In the case of $\psi = 0°$ no plastic strain is generated. Once the stress path reaches the failure envelope the simulated sample fails without any additional plastic deformation. This behavior is directly linked to the dilatancy angle being zero. The stress path on the failure line is an indication of the developed plastic strain. In a Mohr-Coulomb framework, the developed plastic strain is governed by

the plastic potential function g, more specifically the derivative of the plastic potential function with respect to stress $\frac{dg}{d\sigma}$. The formulation of the plastic potential function g is dependent on the difference in stress, dilatancy angle and cohesion. As this case is isotropic, meaning that the vertical stress σ_{yy} and horizontal stress σ_{xx} are equal, the difference in stress is zero. As listed in Table 1 the cohesion equals zero in this simulation. Consequently, the dilatancy angle is the only parameter that controls the development of plastic strain. This explains why the non-dilatant case shows no development of plastic strain.

In the case of $\psi = \phi$ plastic deformation is generated unlike in the case of $\psi = 0$. This is a direct result of the increase in the dilatancy angle. As mentioned in Chapter 2, the dilatancy angle governs the plastic volumetric strains generated. When the simulation hits the failure envelope ($f = 0$) trial stresses will be generated above the failure envelope ($f < 0$), in the "impossible stress space" as illustrated in Figure 8a. These trail stress will be corrected with the plastic multiplier λ in order to simulate a feasible stress state following the failure line ($f = 0$).

In order to assess the influence of the initial stress state on the mobilized shear strength and the stress path, a normally consolidated sample ($K_0 = 0.5$) is simulated. In this stress state the initial horizontal stress σ_{xx} is half the initial vertical stress σ_{yy}. This variation in initial stress state is introduced to examine how difference in stress influences the development of plastic strain and mobilized shear resistance. As previously stated, the development of plastic strain is governed by the plastic potential function. For a cohesionless material, this function is dependent on the stress difference and the dilatancy angle ψ.

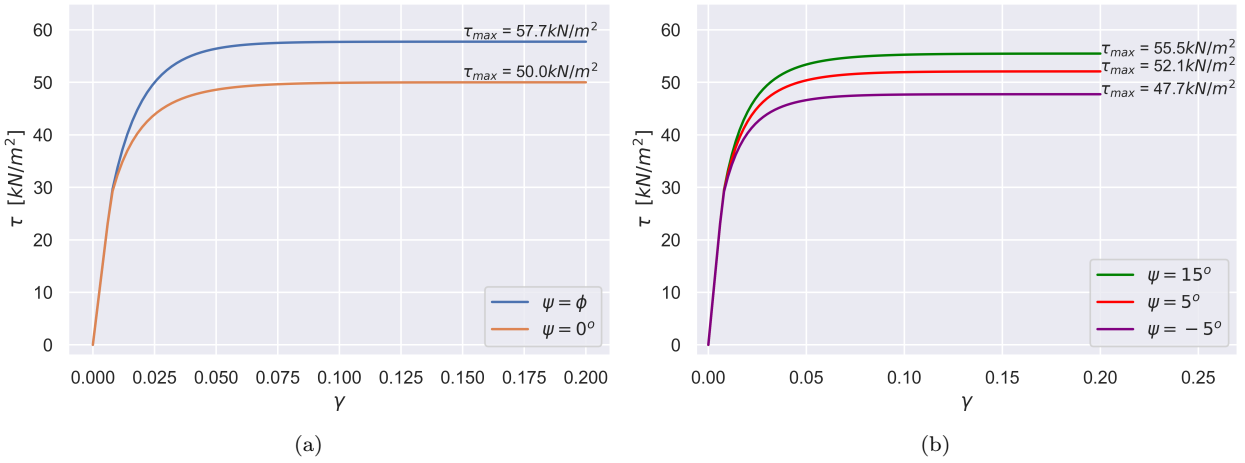

(a) (b)

Figure 13: Shear stress - shear strain relation from a DSS test simulation with $\phi = 30°$ and $K_0 = 0.5$ for the case of: (a) $\psi = \phi$ and $\psi = 0°$; (b) $\psi \neq \phi$

To assess the influence of the difference in stress on the mobilized shear strength and plastic deformation, simulations are performed with a different value of K_0. This parameter, defined as the ratio between the initial vertical and horizontal stress, is now be set to 0.5. This means that the initial horizontal stress σ_{xx} is now half the initial vertical stress σ_{yy}. As a result, the initial stress state becomes anisotropic and the difference between principal stresses is no longer zero. Figure 13 illustrates the mobilized shear strength for $0° \leq \psi \leq \phi$ with $\phi = 30°$ and $K_0 = 0.5$. In this simulation the sample no longer shows a linearly elastic-perfectly plastic Mohr-Coulomb behavior. This is an effect of stress rotation during shear. Despite the change in stress state, the residual mobilized shear strength remains unaffected by the value of K_0, provided the initial vertical stress σ_{yy} is held constant. In every case of $0° \leq \psi \leq \phi$, the peak in the mobilized shear strength is primarily governed by the dilatancy angle ψ. However, the initial stress anisotropy introduced by varying K_0 does influence the stress path, particularly in terms of the amount of plastic strain generated during loading.

The corresponding simulated stress paths of the normally consolidated sample, imposed with $K_0 = 0.5$, are illustrated in Figure 14. A similar overall trend is observed in the stress path when compared to the isotropic case. In the case of $\psi = 0°$, less plastic strain is simulated than in the case of $\psi = \phi$, as expected due to

the dilatancy angle being set to zero. However, unlike the isotropic case this non-dilatant case ($\psi = 0°$) does show development of plastic strain. This is a direct effect of the non-zero difference is stress. As previously discussed, the development of plastic strain is determined through the derivative of the plastic potential function with respect to stress. For a cohesionless material, this gradient is influenced by both the dilatancy angle ψ and the difference between stresses. Since the stress difference in this case is non-zero, plastic deformation occurs even when $\psi = 0°$, demonstrating the influence of stress anisotropy on plastic flow behavior.

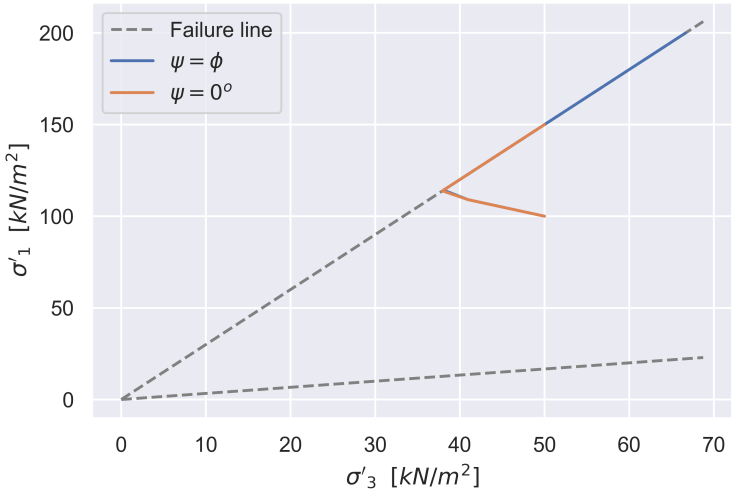

Figure 14: Stress path from a DSS test simulation with $\phi = 30°$ and $K_0 = 0.5$ for the case of $\psi = \phi$ and $\psi = 0°$

It is important to note that Figure 14, which illustrates the simulation with $K_0 = 0.5$, also shows the final stress states. In the case of $\psi = 0°$, the simulation shows a final stress state of $\sigma_1 = 150kN/m^2$ and $\sigma_3 = 50kN/m^2$. For the case of $\psi = \phi$, the final stress state is $\sigma_1 = 200kN/m^2$ and $\sigma_3 = 66.6kN/m^2$. These final stress conditions are consistent with those obtained in the isotropic simulations ($K_0 = 1$). This indicates that the initial stress ratio K_0, when applied with constant vertical stress σ_{yy}, does not affect the final stress state.

In Figure 15a a DSS simulation of an overconsolidated sample is illustrated, imposed with initial stress ratio $K_0 = 1.5$. In this simulation, the initial horizontal stress σ_{xx} is larger than the initial vertical stress σ_{yy}. The maximum mobilized shear strength in both cases of $\psi = \phi$ and $\psi = 0°$ is identical to the simulations imposing $K_0 = 1$ and $K_0 = 0.5$. This confirms that the initial stress state, governed by the value of K_0, does not influence the maximum shear strength. Instead, the mobilized shear strength is solely governed by the dilatancy angle ψ, when keeping the friction angle ϕ constant. Interestingly, in the case of $\psi = 0°$ a peak shear strength can be observed, which is equal to the shear strength in the case of $\psi = \phi$. The softening behavior that can be observed after the peak resistance in the case of $\psi = 0°$ is caused by stress rotation.

In reality, a dense sand will dilate significantly at yield. This plastic dilation will create a looser sand, which results in material degradation leading to a reduction in the friction angle. This material degradation is not incorporated in the model, as the friction angle is kept constant. This simulation assumes perfect plasticity, meaning that the strength parameters remain constant during yielding (Teunissen, 2007). The softening behavior is the result of a decrease in horizontal stress σ_{xx}. This phenomenon is referred to as non-associated softening, and only occurs in the case of a non-associative flow rule $g \neq f$ (Vermeer, 1990).

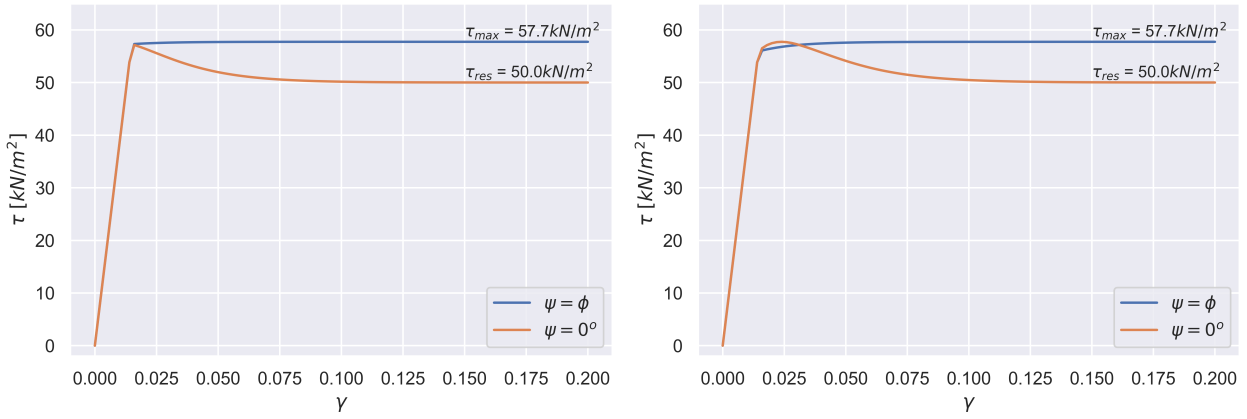

(a) (b)

Figure 15: Shear stress - shear strain relation from a DSS simulation with $\phi = 30°$ and $\psi = 0°; \phi$ imposing: (a) $K_0 = 1.5$; (b) $K_0 = 2.0$

The stress paths corresponding to the two overconsolidated simulations in Figure 15 are illustrated in Figure 16. Interestingly, these simulations generated more plastic deformation in the case of $\psi = 0°$ compared to the case of $\psi = \phi$. This outcome is in contradiction with the literature, as it is stated that a higher dilatancy angle ψ will result in a higher degree of plastic deformation. This is a direct result of the initial stress states, governed by K_0. It is important to note that the final stress states illustrated in Figure 16 remain unchanged compared the previous simulations. This is because the final stress state is not influenced by K_0, provided the initial vertical stress σ_{yy} is kept constant. The case of $\psi = 0°$ shows a final stress state of $\sigma_1 = 150kN/m^2$ and $\sigma_3 = 50kN/m^2$. In the case of $\psi = \phi$ the simulation shows a final stress state of $\sigma_1 = 200kN/m^2$ and $\sigma_3 = 66.6kN/m^2$. Only the initial stress state changes, as this is governed by K_0, which influences the starting point of the stress path. The evolution of the stress path itself is determined through both the yield function f and the plastic potential function g. The fact that the stress path will have to reach the unchanged final stress path from varying initial conditions partly explains the behavior shown in Figure 15.

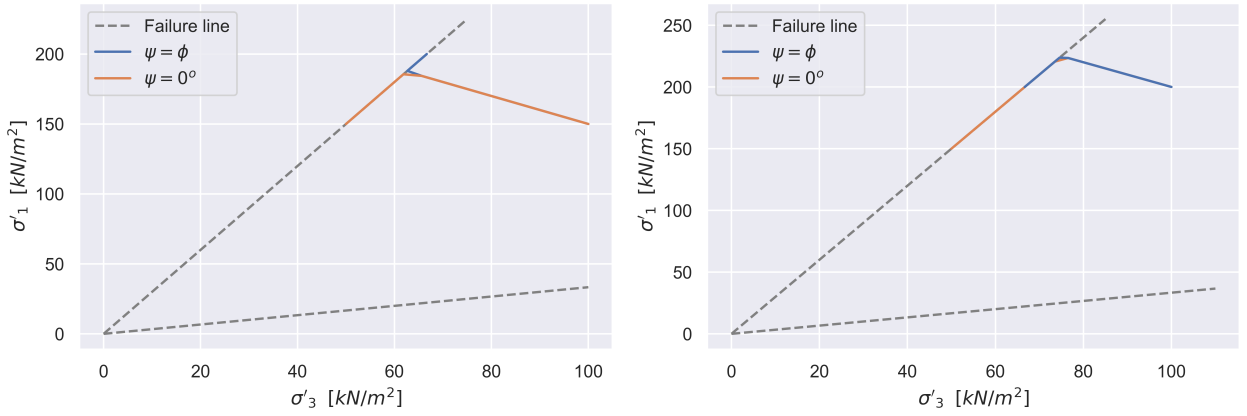

(a) (b)

Figure 16: Stress paths from a DSS test simulation with $\phi = 30°$ and $\psi = 0°; \phi$ imposing: (a) $K_0 = 1.5$; (b) $K_0 = 2.0$

The influence of the initial stress state on the mobilized shear strength is more clearly illustrated in Figure 17. For the case of $\psi = \phi$ (Figure 17a), no peak resistance is observed and the maximum shear strength in the simulation follows the classical Coulomb equation with the $\tan\phi$ relation. In contrast, for the case of $\psi = 0°$ (Figure 17b) the simulation shows a peak shear strength dependent on the initial stress state of the sample. Specifically, for an overconsolidated sample the simulation shows a peak shear strength equal

to the classical Coulomb equation, but reduces to a residual shear strength equal to the Davis approach for non-dilatant material following the $\sin\phi$ relation.

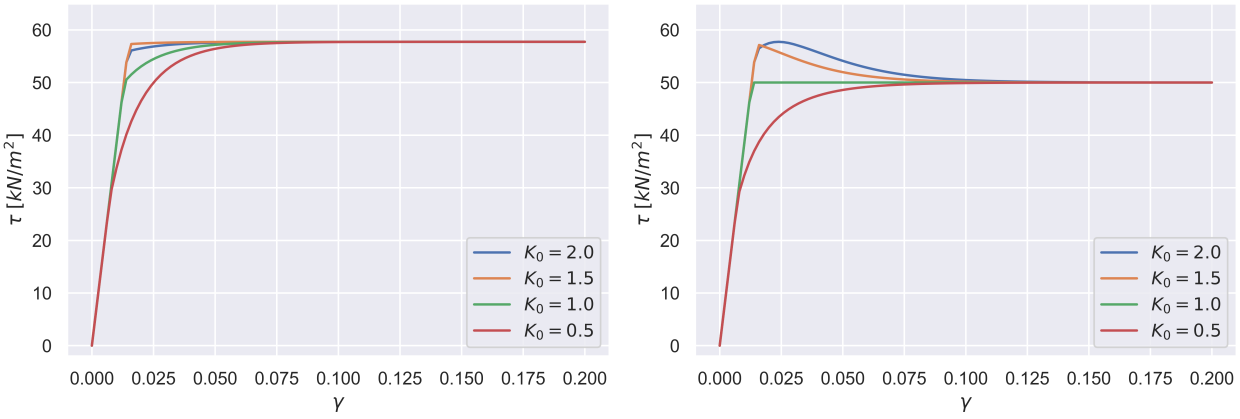

(a) (b)

Figure 17: Shear stress - shear strain relation from a DSS simulation with $\phi = 30°$ and varying initial stress states imposed by K_0 for the case of: (a) $\psi = \phi$; (b) $\psi = 0°$

It is important to note that the Mohr's circles corresponding to the final stress state in each simulation shift to the right with increasing dilatancy angle ψ. This shift is due to the increased maximum strength τ as a result of an increase in dilatancy angle ψ. The failure envelope remains unchanged across all cases of ψ and K_0, as the friction angle ϕ is held constant. The failure line represents the Coulomb failure envelope, which is governed by the friction angle ϕ and cohesion c. Since the simulations concern dense cohesionless sand, the cohesion c is irrelevant as this is set to zero. The increase in strength affects the radius of the circle which has to fit under the failure line, as stresses above the failure line are impossible. As a result of this the Mohr circle shifts to the right. The simulations with $K_0 = 0.5$, $K_0 = 1$ and $K_0 = 1.5$, the Mohr's circles of the final stress state are identical. This highlights that the initial stress ratio K_0 does not affect the final strength condition when the initial vertical stress σ_{yy} is kept constant.

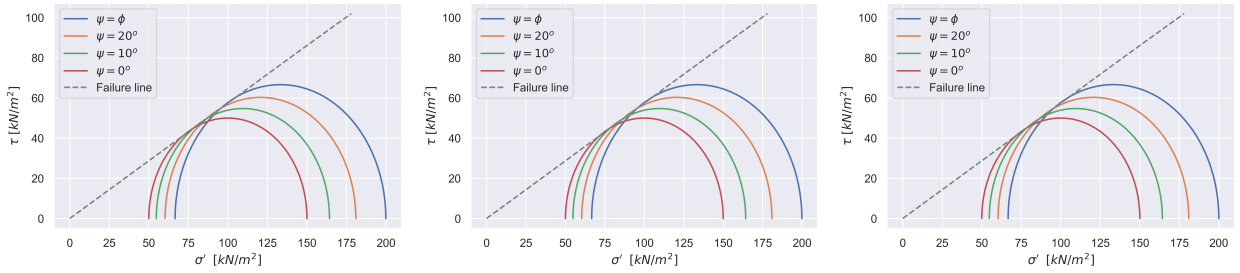

(a) (b) (c)

Figure 18: Mohr's circles of the final stress state from the DSS test simulation with $\phi = 30°$ imposing different initial stress conditions: (a) $K_0 = 0.5$; (b) $K_0 = 1.0$; (c) $K_0 = 1.5$

In summary, numerical simulations of a DSS test demonstrated that the dilatancy angle ψ is the primary factor governing the mobilized shear strength, independent of the initial stress state imposed by K_0. The results validated that the case of $\psi = 0°$ satisfies the classical Coulomb equation following the $\sin\phi$ relation. The case of $\psi = \phi$ satisfies the Davis approach for non-dilatant material following the $\tan\phi$ relation. For any case in between $0 < \psi < \phi$ the Davis expression for dilatant material will hold. While ψ controls the peak shear strength, the initial stress state imposed by K_0 influences the stress path, degree of stress rotation, and the amount of plastic deformation generated during loading. Simulations with different K_0 values revealed that the final stress state remains unchanged when the initial vertical stress σ_{yy} is kept constant, meaning the mobilized strength is unaffected by the initial stress state. However, the evolution of the stress path and the developed plastic strain is sensitive to the difference in stresses caused by variations in K_0. An

overconsolidated non-associated material ($K_0 > 1$; $\psi = 0°$) shows a peak Coulomb resistance followed by a residual Davis resistance. This is known as non-associated softening (Vermeer, 1990). A normally consolidated non-associated samples ($K_0 < 1$; $\psi = 0°$) do not show softening but instead mobilize a residual Davis strength directly. Associated material ($\psi = \phi$), showed a peak Coulomb resistance with no softening behavior regardless of the initial stress state. The Mohr's circles of the final stress states consistently shift to the right with increasing ψ, reflecting higher shear strength, while the failure envelope defined by ϕ and zero cohesion remains unchanged. These findings confirm that while the dilatancy angle governs the peak mobilized strength, the imposed initial stress ratio K_0 controls the stress path and plastic deformation.

3.2 Slope stability

To evaluate the influence of the dilatancy angle ψ on slope stability, an embankment model is developed in PLAXIS 2D. According to Houlsby (1991), the differences between of associated ($\psi = \phi$) and non-associated ($\psi = 0°$) plasticity are expected to be limited for relatively unconstrained problems, such as slopes. In such conditions, the soil mass is free to deform allowing dilation to occur at yield without significant restraint. As a result, it is anticipated that, other than the strength, the dilatancy angle ψ should have little influence on model outcome. The embankment geometry applied to the model is illustrated in Figure 19. The mesh used in this model consists of 11,350 15-node elements, which is a relatively fine mesh discretization. This level of refinement was chosen because the difference in model outcome between associated and non-associated plasticity becomes more pronounced with increasing mesh refinement. This aspect will be further discussed in Chapter 4.

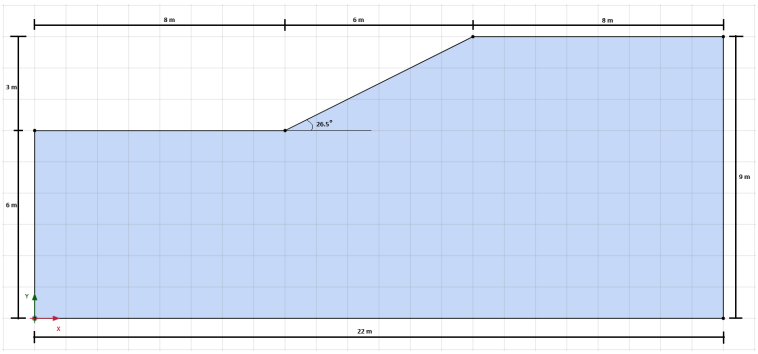

Figure 19: Geometry of the embankment used for the slope stability problem

For this analysis, the Mohr-Coulomb constitutive model is applied. The material parameters, which are representative of a dense sand, are listed in Table 3. Although a dense sand is typically known to be cohesionless, a small cohesion value of 1 kPa is introduced in the model. In simulations with zero cohesion, the failure mechanism develops as a shallow slip surface along the slope. This is not representative of practical slope failures. Including a small cohesion value helps develop a deeper and more realistic failure mechanism, thereby improving the relevance of the simulation results for engineering applications.

Table 3: Material parameters used for the embankment model in the slope stability analysis

Description	Symbol	Value
Unsaturated unit weight	γ_{unsat}	18 kN/m^3
Saturated unit weight	γ_{sat}	20 kN/m^3
Young's modulus	E'_{ref}	15,000 kN/m^2
Poisson's ratio	ν	0.3
Cohesion	c'_{ref}	1 kN/m^2
Friction angle	ϕ	30°
Dilatancy angle	ψ	0°; 30°

The aim of this model is to determine the factor of safety (FoS) and to evaluate the failure mechanism for two scenarios: an associative case ($\psi = \phi$) and a non-dilatant non-associative case $\psi = 0°$. The FoS is

determined using a ϕ/c-reduction method, in which both $\tan\phi$ and c are gradually reduced until the model can no longer maintain equilibrium. In Figure 20 the safety analysis of the embankment in PLAXIS 2D is illustrated for both cases. It should be noted that the absolute magnitude of the displacements shown in the figure is irrelevant. When the FoS stabilizes as the displacement increase, the FoS of the slope has been determined. The results show a higher FoS for the case of $\psi = \phi$, which is due to the higher strength as a result of the increased dilatancy angle. This case allows for greater plastic volumetric deformation before failure occurs, resulting in improved slope stability.

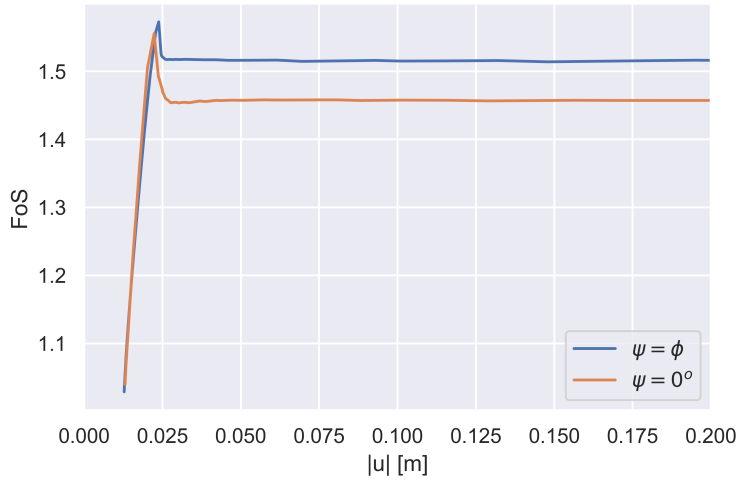

Figure 20: Comparison of the FoS in the slope stability model for the cases of $\psi = \phi$ and $\psi = 0°$

As previously mentioned, in the case of $\psi = \phi$ the soil will show a higher strength at failure, following the $\tan\phi$ relation as defined in Equation 14. In contrast, for the case of non-dilatant non-associated material ($\psi = 0$) the soil will have a lower strength following the $\sin\phi$ relation as defined in Equation 21. The difference between these two relations become more pronounced with mesh refinement, a topic that will be addressed in detail in Chapter 4. Since soil on a slope is able to deform in a relatively unconfined manner the effect of dilation should be limited, apart from its influence on strength. This is supported by the results shown in Figure 21, where the failure mechanisms are similar in both cases. This figure represents a shear strain plot, illustrating the failure mechanism through the development of shear bands. The primary differences are minor shifts in the location of the shear band near the toe and crest of the embankment. Although the output suggests that the case of $\psi = \phi$ shows less plastic deformation in the shear band than in the case of $\psi = 0$, this observation should be interpreted with caution. The deformations shown in a ϕ/c-reduction analysis are not absolute, as they are affected by the numerical step size adopted by PLAXIS during the analysis. Since the method approaches a failure condition in which deformations theoretically become infinite, the step sizes and resulting displacement magnitudes can vary between cases. Therefore, the interpretation should focus on the failure mechanism's shape rather than the absolute values of the deformations.

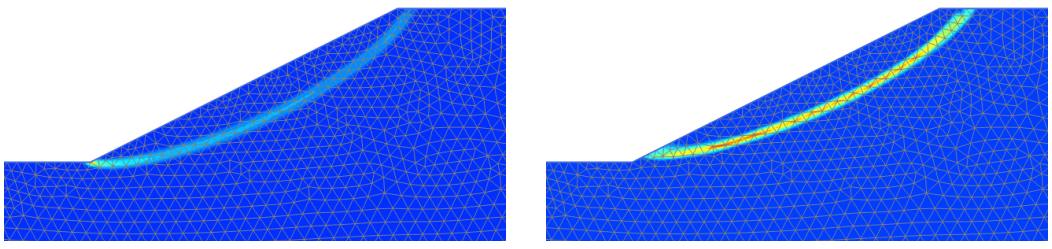

(a) (b)

Figure 21: Shear strain plot showing the shear band formation of the slope stability simulation for the case of: (a) $\psi = \phi$; (b) $\psi = 0$

The movement mechanism of the slope is illustrated in Figure 22 for the case of $\psi = \phi$ and $\psi = 0°$. While the overall movement patterns are similar, the case of $\psi = \phi$ (Figure 22a) shows a movement mechanism that extends deeper into the soil body and further along the slope. This is a result of the volumetric expansion which is controlled by ψ. As ψ increases, the soil will tend to develop more plastic deformation before failure, allowing for greater displacement and a more extensive failure mechanism.

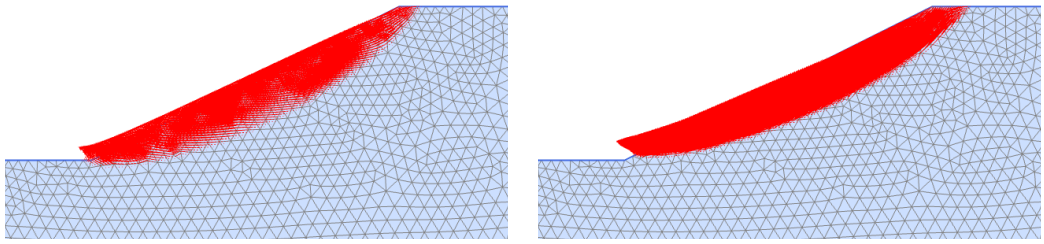

(a) (b)

Figure 22: Incremental displacement showing soil movement of the slope stability simulation for the case of: (a) $\psi = \phi$; (b) $\psi = 0$

In addition to the dilatancy angle ψ, the FoS of a slope is also influenced by the friction angle ϕ itself. In Figure 23 the relation between the dilatancy angle ψ and the FoS for different values of the friction angle ϕ is illustrated. Each curve in the figure represents a different friction angle. For each curve a similar trend can be observed, namely an increasing FoS with increasing ψ. This increase in FoS is a result of the higher strength followed by the $\tan\phi$ relation when $\psi = \phi$. Notably, all curves converge to a nearly constant FoS at a dilatancy angle of approximately 20°, regardless of the friction angle. This suggests that beyond this point, further increases in ψ have a negligible effect on the slope's overall stability.

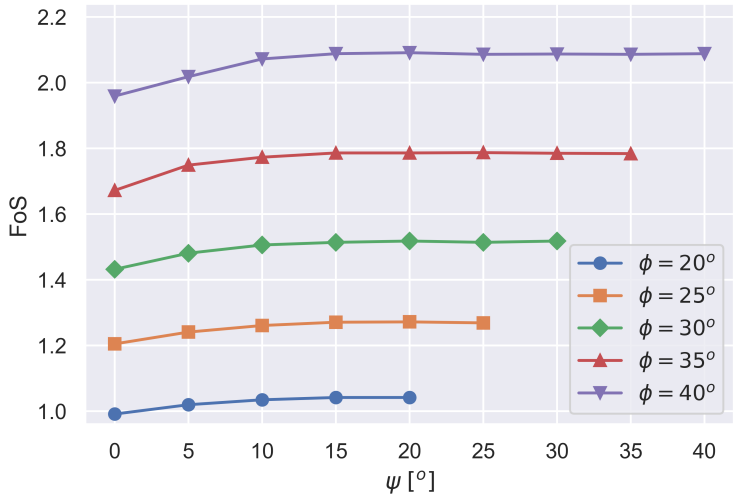

Figure 23: Relation between FoS and dilatancy angle ψ, with varying friction angles ϕ for a slope inclination $\alpha = 26.5°$

The convergence of the model outcome, in terms of FoS, in the slope stability simulations shown in Figure 23 beyond a dilatancy angle of approximately 20° is due to the way PLAXIS determines FoS in non-associated cases ($\psi \neq \phi$). During a PLAXIS ϕ/c-reduction, the friction angle ϕ is incrementally reduced while the dilatancy angle ψ remains fixed. When the reduced, or "mobilized," friction angle decreases to equal the dilatancy angle, both parameters are then reduced simultaneously until equilibrium is no longer maintained. In essence, the model behaves as non-associated until the mobilized friction angle matches the dilatancy angle, after which the parameters become effectively associated. Once the dilatancy angle reaches a certain threshold, the difference between associated and non-associated model outcome disappears because the friction angle must be reduced below the dilatancy angle to cause instability. For example, in the case of

$\psi = \phi$ for the curve with $\phi = 40°$ (purple curve in Figure 23), the FoS was found to be approximately 2.1. Using $\tan \phi_{mob} = \frac{\tan \phi}{FoS}$ according to Equation 23, the mobilized friction angle ϕ_{mob} is calculated as 21.8°. This means that the friction angle must be reduced to this value to destabilize the slope. Therefore, any simulation with a dilatancy angle exceeding about 21.8° will yield the same FoS as an associated plasticity model, independent of the non-associated parameters. Since the slope angle α is kept constant in these simulations, the mobilized friction angle remains roughly the same across different friction angles represented by the various curves. This explains why all curves converge to a constant FoS beyond a dilatancy angle near 20°.

In Table 4, the difference in FoS between the cases of $\psi = \phi$ and $\psi = 0°$ is listed for the different friction angles ϕ. This difference in the FoS is primarily a result of the difference in shear strength, where one case follows the classical Coulomb strength and the other follows the Davis strength for non-dilatant material. As discussed in the literature review, this difference between these strength models increases with increasing friction angle (illustrated in Figure 9). This trend is also reflected in the slope stability simulations, where the difference in FoS is 5.08% for $\phi = 20°$ and 6.74% for $\phi = 40°$.

Table 4: Difference in FoS with varying friction angle ϕ for a slope inclination $\alpha = 26.5°$

	$\psi = \phi$	$\psi = 0°$	$\Delta\%$
$\phi = 20°$	1.042	0.992	5.08%
$\phi = 25°$	1.269	1.205	5.31%
$\phi = 30°$	1.518	1.432	6.01%
$\phi = 35°$	1.784	1.672	6.70%
$\phi = 40°$	2.091	1.959	6.74%

Besides the dilatancy angle ψ and the friction angle ϕ, the FoS is also influenced by the slope inclination α. The relation between the dilatancy angle ψ and the FoS for different slope inclinations is illustrated in Figure 24. Each curve corresponds to a different slope inclination α. A similar trend can be observed across all curves. In every case of $\psi = 0°$ a lower FoS was determined, while in every case of $\psi = \phi$ a higher FoS was determined. This directly follows from the dilatancy angle ψ, which governs the soil strength. Additionally, as the slope inclination increases the FoS decreases for all cases. This figure further confirms that the mobilized friction angle depends on the slope inclination. Holding the friction angle constant while increasing the slope steepness reduces the required mobilized friction angle for instability to occur.

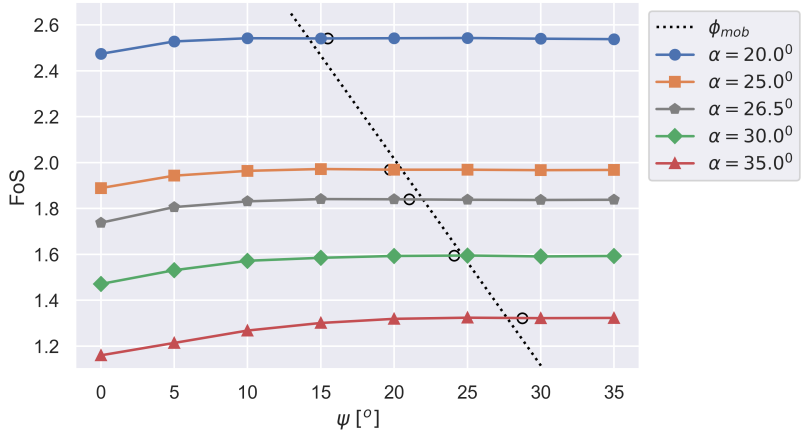

Figure 24: Relation between FoS and dilatancy angle ψ, for varying slope inclinations α with $\phi = 35°$

Figure 24 validates that the value of the dilatancy angle ψ at which the FoS converges to a fixed value depends on the mobilized friction angle ϕ_{mob}. The black hollow dots on each curve in this figure represent the mobilized friction angle corresponding to the specific slope inclinations. A black dotted line connects

these points to better illustrate the influence of the mobilized friction angle. It can be observed that the FoS output converges near the point where each curve intersects this dotted line. This implies that when the dilatancy angle equals the mobilized friction angle, there is no difference in results between associated and non-associated plasticity models, as the parameters effectively become associated during the reduction process. Note that convergence occurs at a ψ slightly less than ϕ_{mob}. This is due to the degree of non-associativity Λ. Because the difference between ψ and ϕ_{mob} is small at this stage, the model outcome will not be very different from that of the associated case.

Table 5: Difference in FoS for varying slope inclination α with $\phi = 35°$

	$\psi = \phi$	$\psi = 0°$	$\Delta\%$
$\alpha = 20°$	2.540	2.474	2.57%
$\alpha = 25°$	1.968	1.889	4.18%
$\alpha = 30°$	1.593	1.471	8.29%
$\alpha = 35°$	1.323	1.160	14.05%

Note that the absolute difference in FoS between the cases of $\psi = \phi$ and $\psi = 0°$ increases with increasing slope inclination α. Table 5 lists this difference for various slope inclinations. At $\alpha = 35°$ the difference reaches 14.05%, whereas at $\alpha = 20°$ it is only 2.57%. As discussed in the literature review, the difference between associated and non-associated plasticity cases increases with increasing friction angle ϕ. With steeper slopes, the friction angle needs to be mobilized less to induce failure, effectively resulting in a higher friction angle. Therefore, the increasing difference is not directly caused by slope inclination itself, but rather by the higher mobilized friction angle.

To summarize, the influence of the dilatancy angle ψ on slope stability was investigated by modeling an embankment in PLAXIS 2D. Theoretically, ψ governs the orientation of the shear band that forms upon failure, which in its turn controls the mobilized shear resistance in a potential slip surface. This concept was initially validated through DSS test simulations, but practical slope stability analysis reveals some nuances. For the slope stability problem, the case of $\psi = 0°$ resulted in a consistently lower FoS compared to the case of $\psi = \phi$. This difference increased with increasing friction angle ϕ, confirming findings from the literature that non-associativity Λ magnifies the discrepancy between model outcomes. However, for intermediate dilatancy angles ($0° < \psi < \phi$), the FoS did not vary continuously but instead converged toward a constant value at around $\psi = 20°$ regardless of the friction angle for a slope inclination of $\alpha = 26.5°$. This convergence behavior arises from the numerical implementation in PLAXIS, which uses a ϕ/c-reduction method to determine the FoS. For non-associated cases, the friction angle ϕ is incrementally reduced while the dilatancy angle ψ remains constant, until both parameters become equal. Beyond this point, ϕ and ψ are reduced simultaneously, effectively shifting the problem to an associated scenario. As a result, for dilatancy angles greater than this threshold the model behaves as if fully associated. This effectively eliminates differences in FoS between associated and non-associated cases. While the dilatancy angle plays a crucial role in governing the strength and deformation behavior of soil in slope stability problems, numerical settings and boundary conditions strongly influence the observed effect of ψ on model outcome.

3.3 Retaining structure

In this section, the influence of the dilatancy angle ψ is further investigated using a retaining structure model. According to Houlsby (1991), the difference between associated and non-associated plasticity becomes more pronounced as deformation becomes increasingly confined and constrained. This makes retaining structures an ideal case to study the role of dilation under restricted deformation conditions. The retaining structure problem is modeled as illustrated in Figure 25. To accurately capture model outcome, a mesh consisting of 26,204 15-node elements is applied for the retaining structure simulations. As the difference between associated and non-associated flow tend to become more nuanced with increasing mesh refinement. The influence of mesh refinement on this behavior will be discussed in detail in the following chapter.

The geometry of the retaining structure model is shown in Figure 25. The model is constructed under plane strain conditions to represent a typical 2D cross-section of a construction pit. In the figure, the blue vertical line represents the retaining wall. Attached to this wall are green lines marked with "+" and "-", which

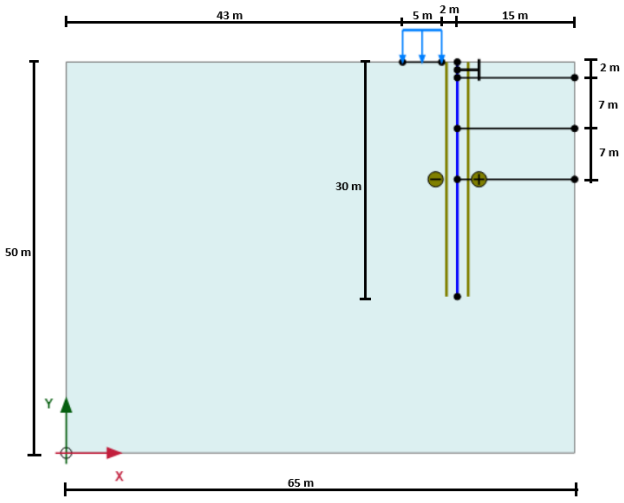

Figure 25: Geometry of retaining structure model

represent the positive and negative interface elements used to simulate the soil–structure interaction. The rotated "T" symbol at the top of the wall indicates the anchor connection, providing lateral support to the structure. On the right side of the figure, the black-outlined boxes indicate the soil volume that will be excavated during the simulation. The right boundary of the model is treated as a symmetry axis, meaning only half of the construction pit is modeled to reduce computational effort while maintaining accuracy.

Table 6: Soil properties used for the retaining structure model

Description	Symbol	Value
Unsaturated unit weight	γ_{unsat}	18 kN/m^2
Saturated unit weight	γ_{sat}	20 kN/m^2
Young's modulus	E'_{ref}	20,000 kN/m^2
Poisson's ratio	ν	0.25
Cohesion	c'_{ref}	0.01 kN/m^2
Friction angle	ϕ	35°
Dilatancy angle	ψ	0°; 35°

The soil and structural properties used in the retaining structure model are listed in Table 6 and Table 7, respectively. A parameter set resembling a relatively stiff soil is used in this simulation. This choice ensures that the soil mass bears a significant portion of the applied load, which results in greater stress redistribution and strain development in the soil mass itself. As a result, the simulations yields clearer patterns in the shear strain plots. These plots, which visualize the formation of shear bands, provide valuable insight into the failure mechanism simulation by the model. This is essential for effectively assessing the influence of the various parameters investigated in this study.

Table 7: Structural element properties used for the retaining structure model

	Description	Symbol	Value
Retaining structure	Unit weight	w	8 $kN/m/m$
	Axial stiffness	EA	$5 \cdot 10^6$ kN/m
	Bending stiffness	EI	$5 \cdot 10^5$ kNm^2/m
	Poisson's ratio	ν	0.2
Anchor	Spacing	$L_{spacing}$	5 m
	Axial stiffness	EA	$5 \cdot 10^6$ kN/m
	direction x	-	15 m

The shear strain distribution from the retaining structure simulations is illustrated in Figure 26 for both cases of $\psi = \phi$ and $\psi = 0°$. These shear strain plots visualize the formation of shear bands, which serve as a clear representation of the failure mechanism in each scenario. As anticipated, the failure mechanisms are very different between the cases of $\psi = \phi$ and $\psi = 0°$. The literature review highlighted that the influence of the dilatancy angle becomes more pronounced in problems where deformation is highly confined or constrained, such as retaining structures. In the case of $\phi = 0°$, distinct and well-defined shear bands develop on both the active and passive side of the wall. At first glance, the case of $\psi = \phi$ shows no distinct shear band formation in Figure 26a. However, a more detailed inspection of the shear strain contours (Figure 27) reveals the presence of a local failure mechanism.

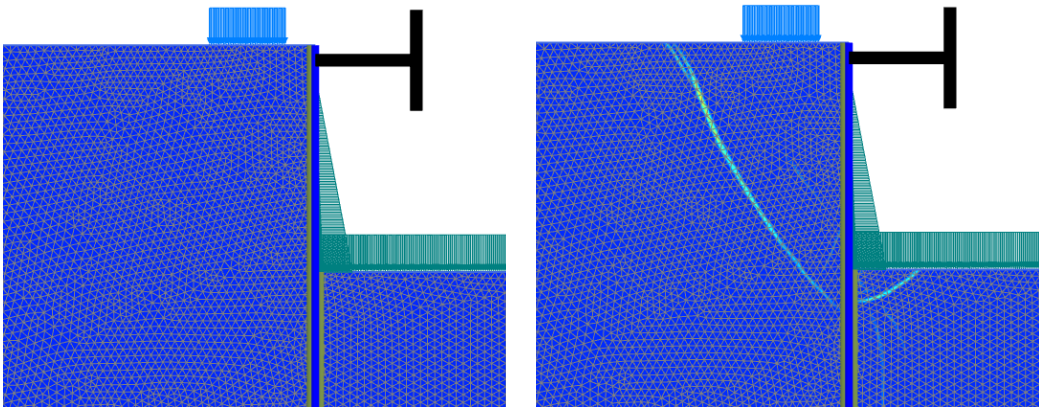

(a) (b)

Figure 26: Shear strain plot showing shear band formation in the retaining structure simulation for the case of: (a) $\psi = \phi$; (b) $\psi = 0$

Figure 27 shows a zoomed-in view of the shear strain distribution for the case of $\psi = \phi$, focusing on the passive side of the retaining structure. This detailed vied reveals the simulated failure mechanism more clearly. The highest concentration of shear strain is observed near the bottom of the excavated zone, which corresponds to the location where the retaining structure exerts the greatest pressure on the soil at the passive side. This zone experiences the most significant stress changes due to the force imposed by the wall. Given the high dilatancy angle in this simulation ($\psi = \phi$), the soil tends to expand as it deforms plastically. However, this dilation is constrained by the retaining structure. The inability of the soil to expand in response to loading leads to failure in this confined zone.

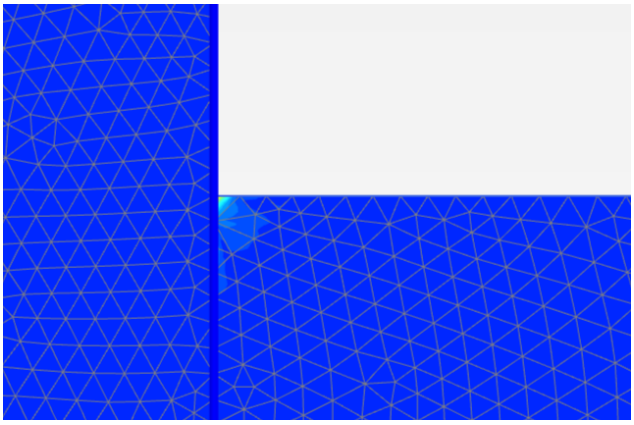

Figure 27: Shear strain plot zoomed in on the passive side of the retaining structure, showing the local failure mechanism for the case of $\psi = \phi$

The incremental displacements generated in the final phase of the retaining structure simulation is illustrated in Figure 28 for the cases of $\psi = \phi$ and $\psi = 0°$. These displacement plot provide insight on the overall

deformation behavior of the soil mass. For the case of $\psi = 0°$, the largest displacements are observed along the active and passive sides of the retaining structure, particularly concentrated near the shear bands. In contrast, for the case of $\psi = \phi$ the displacements are predominantly concentrated on the passive side near retaining structure. This is consistent with the observed shear strain distribution (Figure 27), where soil dilation is most pronounced but also most restricted. The contrast in displacement patterns between the two cases further highlights the influence of the dilatancy angle on deformation behavior in confined geotechnical problems.

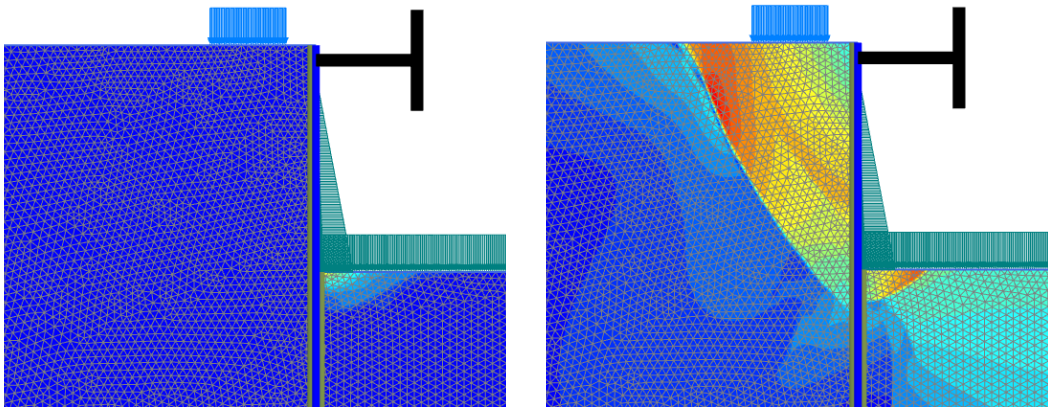

(a) (b)

Figure 28: Incremental displacements for the retaining structure in the case of: (a) $\psi = \phi$; (b) $\psi = 0°$

In Figure 29 the incremental displacement is visualized using arrows, zoomed in on the passive side of the retaining structure for the case of $\psi = \phi$. This figure validates the simulated failure mechanism. The displacement arrows indicate that the soil is being pushed away by the retaining structure. Due to the high dilatancy angle, the soil tends to expand upon loading. However, this dilation is constrained by the retaining structure, resulting in failure.

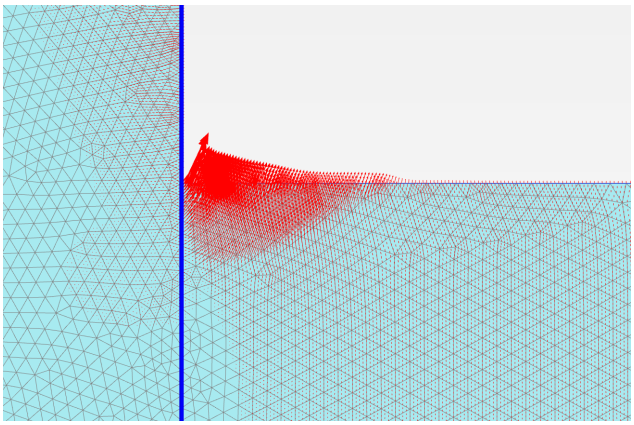

Figure 29: Incremental displacement plot zoomed in on the passive side of the retaining structure, showing the local movement mechanism in the case of $\psi = \phi$

In addition to influencing the failure mechanism, the dilatancy angle ψ also affects the displacements, forces and bending moment of the retaining structure. For consistency, this report will focus on the bending moment, which provides a clear indication of the influence of the different parameters investigated in this research. The simulated bending moment along the retaining structure is illustrated in Figure 30. The positive bending moment is caused by the soil on the active side pressing against the retaining structure. In the case of $\psi = 0°$, this positive bending moment is higher compared to the case of $\psi = \phi$. As the strength of the soil is lower in the case of $\psi = 0°$, the retaining structure will bear a larger share of the load. This

will result in an increase in bending moment along the retaining structure. A similar effect of reduced soil strength was also observed in the slope stability simulations. In the case of $\psi = \phi$, the negative bending moment is higher compared to the case of $\psi = 0°$. This is caused by the failure mechanism characteristic of the high dilatancy case. As mentioned earlier, the retaining structure exerts the greatest pressure against the top of the excavated soil. Because the soil has a high dilatancy angle, it tends to expand upon failure. This volumetric expansion generates a significant bending moment at this location along the retaining structure. Since this failure mechanism is dominant only when $\psi = \phi$, it explains why the negative bending moment is higher in that case.

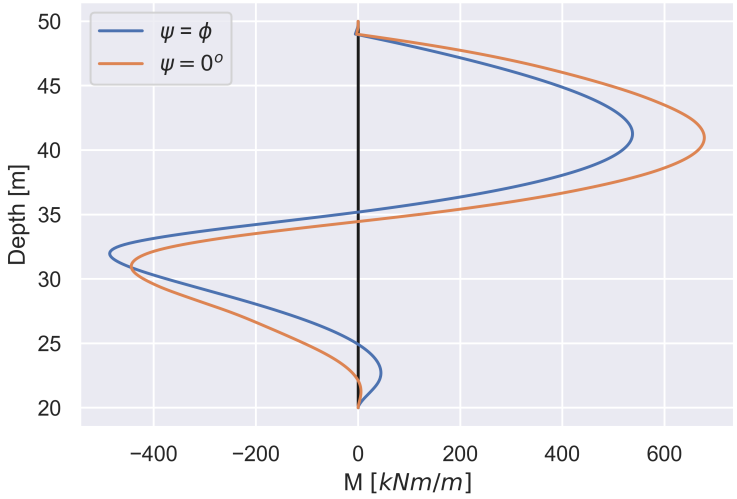

Figure 30: Bending moment of the retaining structure for the cases of $\psi = \phi$ and $\psi = 0°$

Figure 31 illustrates the influence of the friction angle ϕ on the bending moment in the retaining structure. Each curve represents a different friction angle and includes simulations for every case within the range of $0° \leq \psi \leq \phi$. When examining the positive bending moment in Figure 31a, a similar trend can be observed as the slope stability simulations. Specifically, comparing the two extremes $\psi = \phi$ and $\psi = 0°$ shows that the case of $\psi = \phi$ results in a lower positive bending moment, whereas the case of $\psi = 0°$ results in a higher bending moment. This is due to the higher strength of the soil in the case of $\psi = \phi$, allowing it to carry a greater portion of the load. In contrast, the weaker non-dilatant soil ($\psi = 0°$) causes the retaining structure to bear more of the load, leading to increased bending moments.

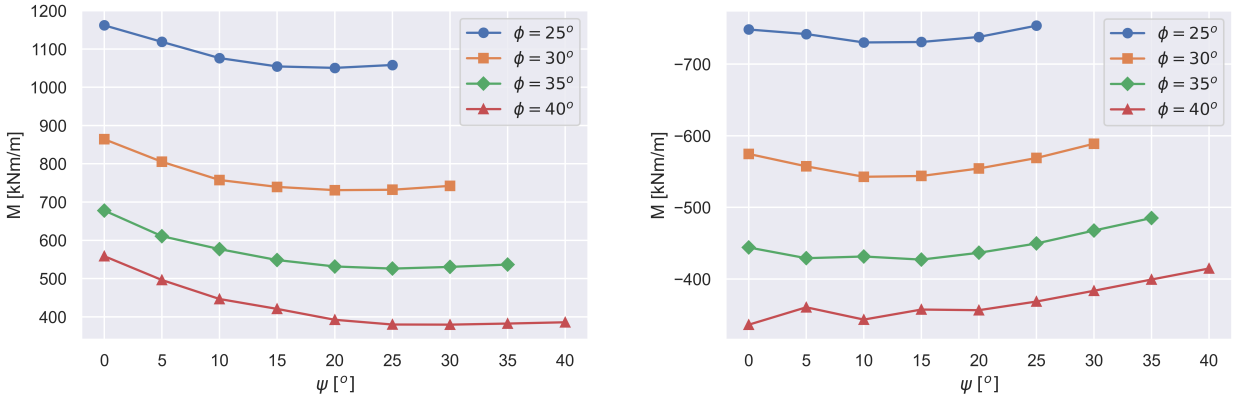

(a) (b)

Figure 31: Influence of the friction angle ϕ on model outcome in the retaining structure simulations in terms of: (a) Positive bending moment; (b) Negative bending moment

Interestingly, in contrast to the slope stability simulations, the intermediate cases $0° < \psi < \phi$ shows a dip in bending moment that was not previously observed. The negative bending moment shows a similar trend, initially decreasing and then increasing with increasing dilatancy angle ψ. These dips are a direct consequence of the changing failure mechanisms in the simulations.

To gain a better understanding of this phenomenon, the bending moment of the retaining structure for different values of ψ with constant ϕ is illustrated in Figure 32. For the positive bending moment, a decrease is observed from $\psi = 0°$ up to $\psi = 25°$. From $\psi = 25°$ to $\psi = \phi$ there is an increase in positive bending moment, as observed in Figure 31a and Figure 32. A similar trend is found in the negative bending moment of the retaining structure. In the negative bending moment there is an initial increase in moment from $\psi = 0°$ to $\psi = 5°$, which is followed by a decrease in moment from $\psi = 5°$ to $\psi = \phi$. These non-linear responses are linked to the developed failure mechanisms, which shift as a results of an increase in the dilatancy angle ψ.

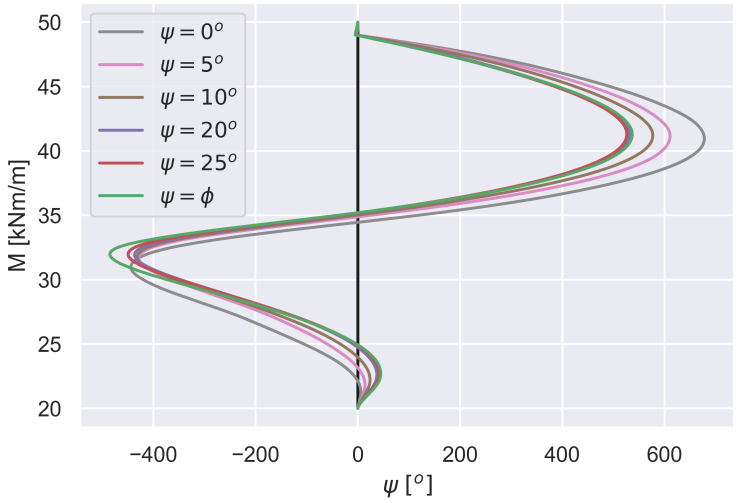

Figure 32: Influence dilatancy angle ψ on the bending moment of the retaining structure with $\phi = 35°$

Figure 33 illustrates the failure mechanisms corresponding to the cases plotted in Figure 32. These figures show the shear strain plots in logarithmic scale for varying dilatancy angle ψ, with the friction angle ϕ kept constant. It can be observed that starting after a dilatancy angle of approximately $\psi = 5°$, the shear bands begin to concentrate on the passive side of the retaining structure. The shear strain plots start to show darker contouring as the passive side. This shift in the failure mechanism explains the trend observed in the negative bending moment beyond $\psi = 5°$, the failure mechanism becomes increasingly dominant on the passive side, resulting in an increasing magnitude of the negative bending moment (i.e. the bending moment becomes more negative). As the dilatancy angle increases further, and reaches $\psi = 25°$, the failure mechanism becomes localized near the top of the excavated soil on the passive side. At this point, the dilative behavior of the soil is significant enough to cause pronounced expansion, leading to a distinct failure mechanism. The resulting soil expansion causes a strong force against the retaining structure in this region, increasing the negative bending moment to such an extent that it must be counteracted by an increase in the positive bending moment. This interaction explains the non-linear behavior observed in the positive bending moment curve beyond $\psi = 25°$.

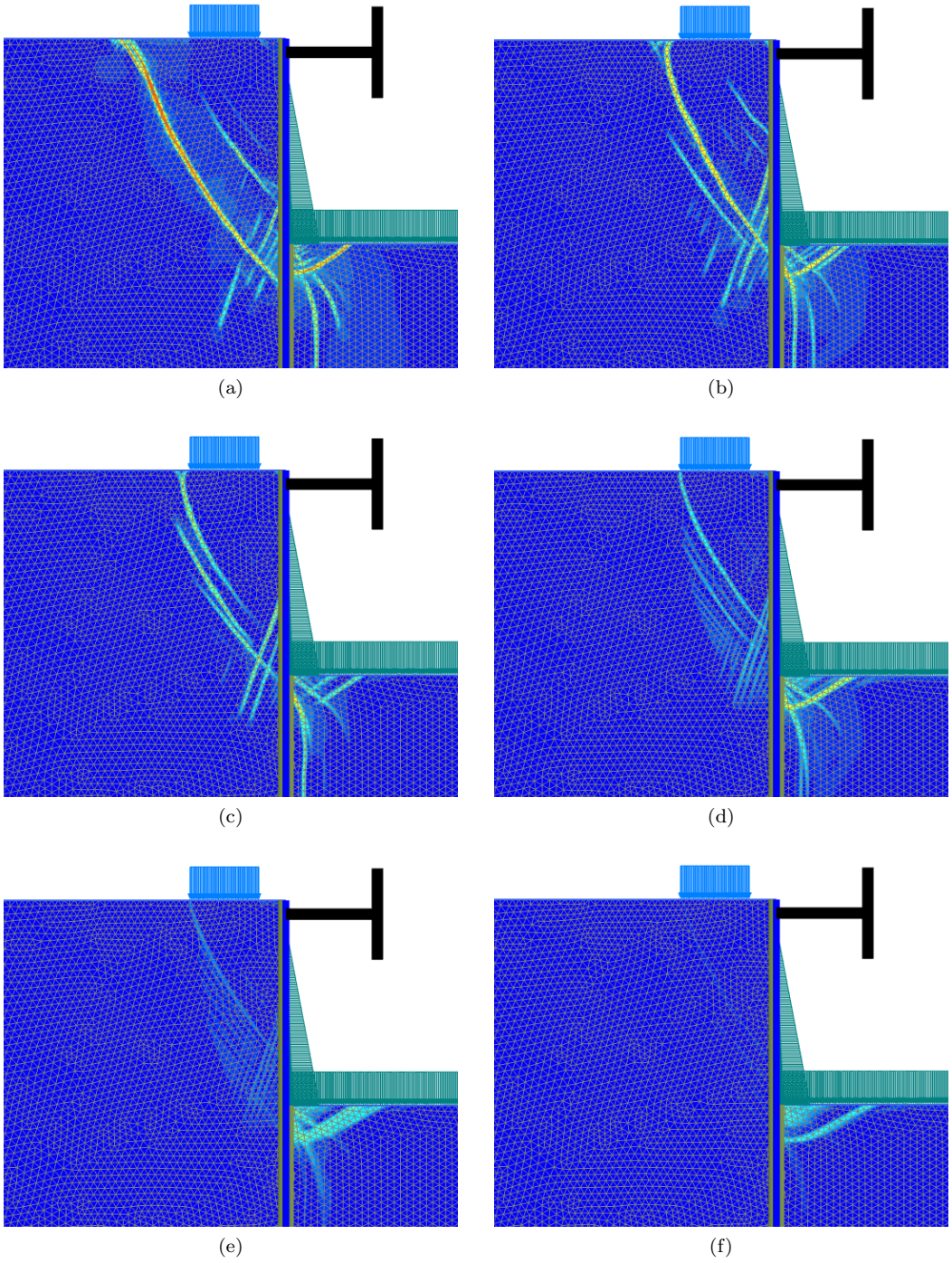

Figure 33: Influence of the dilatancy angle ψ on the failure mechanism (logarithmic scale) for the retaining structure model keeping the friction angle constant at $\phi = 35°$ for the case of: (a) $\psi = 0°$; (b) $\psi = 5°$; (c) $\psi = 10°$; (d) $\psi = 20°$; (e) $\psi = 25°$; (f) $\psi = \phi$

To summarize, in the retaining structure simulations the influence of the dilatancy angle ψ on the failure mechanism and bending moment was assessed. The model was designed with a relatively flexible retaining structure and stiff soil to ensure that the soil body carried most of the load, allowing for clear visualization of the failure mechanism through shear strain plots. Results showed a significant difference in the failure mechanism between the cases of $\psi = \phi$ and $\psi = 0°$. In the non-associated case, shear bands developed on both the active and passive sides, while in the associated case, failure localized at the top of the excavated passive side due to restricted dilation. The bending moments further demonstrated the effect of dilation. A lower

strength in the case of $\psi = 0°$ resulted in higher positive bending moments, as the retaining structure had to resist more soil load. In contrast, the case of $\psi = \phi$ led to higher negative bending moments. Interestingly, intermediate values of ψ ($0° < \psi < \phi$) revealed non-linear trends in bending moments, showing peaks not observed in previous sections. These were linked to shifting failure mechanisms, where at low ψ failure was more distributed, while at higher ψ failure became localized on the passive side. This transition explains the observed peaks in both positive and negative bending moments. Overall, the simulations confirmed that dilatancy plays a crucial role in confined problems like retaining structures, not only in strength but also in determining the failure mechanism.

4 Mesh dependency

Using non-associated plasticity in FEM will lead to numerical instability, non-uniqueness and localization, which will result in a mesh dependent outcome. In contrast, when associated plasticity is applied, the model outcome tends to be consistent under mesh refinement. As highlighted in the previous chapter, the dilatancy angle ψ plays a significant role in influencing model outcome, particularly in problems where the soil deformation is constrained. Therefore, this chapter will discuss the same two problems, slope stability and a retaining structure, to investigate the extent of mesh dependency in model outcome in the case of associated ($\psi = \phi$) and non-associated plasticity ($\psi = 0°$).

4.1 Slope stability

The slope stability model previously discussed in Chapter 3.1 is used in this section to evaluate the mesh dependence in model outcome the case of associated ($\psi = \phi$) and non-associated plasticity ($\psi = 0°$). As in the previous chapter, the model outcome will be measured in terms of factor of safety (FoS). In addition to model outcome, the simulated failure mechanisms for both plasticity formulations will be analyzed, with particular attention to how they are influence by mesh density and the magnitude of the dilatancy angle ψ. The geometry of the embankment is illustrated in Figure 19 and the soil properties are listed in Table 3, which can be found in Chapter 3.1.

The degree of mesh refinement is illustrated in Figure 34. Figure 34a shows the coarsest mesh, consisting of 118 elements, and Figure 40b shows the finest mesh, containing 46,420 elements. The mesh elements generated in PLAXIS are high-order 15-node triangles with 4th-order interpolation of displacements.

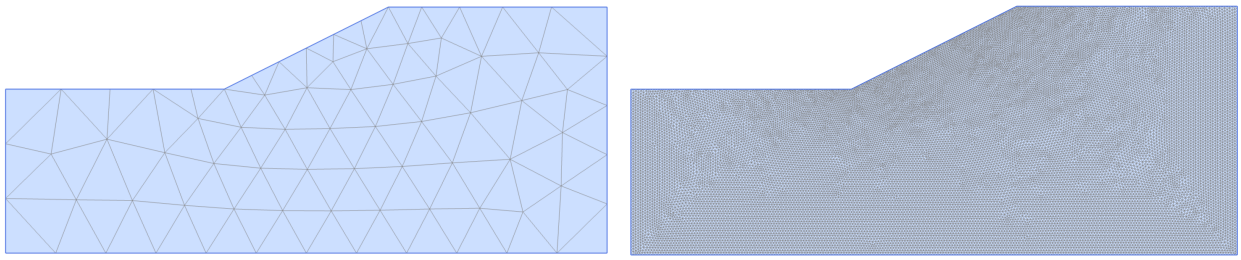

(a) (b)

Figure 34: Degree of mesh refinement applied in the slope stability model: (a) Coarsest mesh consisting of 118 elements; (b) Finest mesh consisting of 46,240 elements

Given the relatively simple geometry of this model, no local mesh refinement was applied. Instead, the global mesh coarseness was incrementally reduced across the entire geometry. For more complex geometries local mesh refinement is recommend to reduce computation time. A practical approach is to first run the model using the "very fine" mesh preset in PLAXIS to identify the formed failure mechanism. Based on the failure mechanism, the mesh can the be locally refined to enhance the accuracy of model outcome while limiting overall computation time.

The relation between mesh density and FoS is presented in Figure 35. In the case of $\psi = \phi$, the FoS is not strongly dependent on the mesh density. Some convergence at very coarse meshes can be observed, as a very coarse mesh will not allow to capture the slip plain accurately. In contrast, the case of $\psi = 0°$ shows a pronounced mesh dependence, with the FoS decreasing approximately 8.5% as the mesh is refined. This sensitivity is caused by localization, a known issue in non-associated plasticity. With increasing mesh refinement the FoS appears to converge, showing a variation of about 1.4% in the post-converged range.

Notice that the difference in FoS between the case of $\psi = \phi$ and $\psi = 0°$ becomes more pronounced with mesh refinement, eventually hitting a plateau at 10,000 elements in this particular geometry. At convergence, the difference in terms of FoS between the cases $\psi = \phi$ and $\psi = 0°$ is approximately 7%.

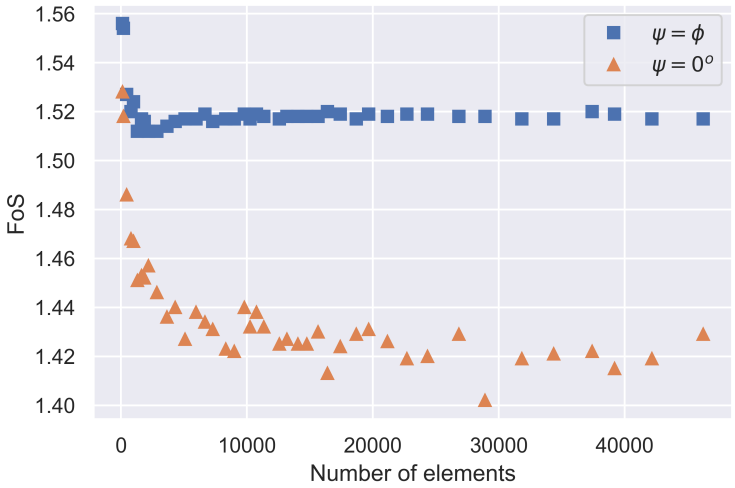

Figure 35: Effect of mesh refinement on model outcome in terms of FoS for a slope stability simulation in the case of $\psi = \phi$ and $\psi = 0°$

In PLAXIS, a preset mesh density can be selected without manually adjusting the coarseness factor in the geometry. Figure 36 highlights the output corresponding to the "very fine" mesh, which contains 796 elements in this particular geometry. As the name suggests, this mesh is generally considered to be sufficiently refined to produce mesh independent results. In the case of $\psi = \phi$ this hold true, as the output shows a FoS of 1.52 corresponding to the "very fine" mesh and remains unchanged with further mesh refinement. However, in the case of $\psi = 0°$ the output has not yet converged at the "very fine" mesh. In this case the FoS is 1.47 for the "very fine" mesh and eventually reducing to 1.42 with mesh refinement. This observation demonstrates that the conventionally accepted "very fine" mesh is not adequate when using non-associated plasticity, due to the increased sensitivity to mesh refinement.

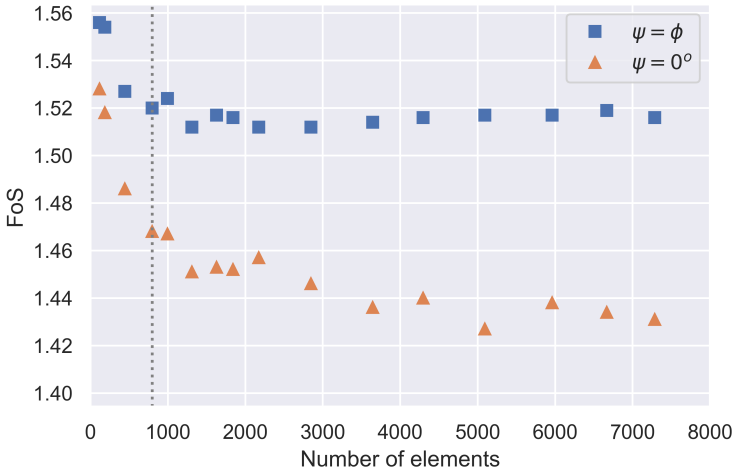

Figure 36: Highlighted model outcome of the slope stability simulation for the "very fine" mesh preset in PLAXIS for the case of $\psi = \phi$ and $\psi = 0°$

Figure 37 illustrates the influence of the friction angle ϕ on the convergence behavior of the slope stability simulations. The curves in this figure represent different values of ϕ, ranging form 20° to 40°. Each curve corresponds to a non-dilatant and non-associated case, where the dilatancy angle is set to zero ($\psi = 0°$). The simulation were performed with mesh densities ranging from 55 to 19,673 elements. Refinement was stopped at 19,673 elements, as further increases in mesh density had negligible influence on model outcome. The results indicate that the number of elements required for convergence is independent of the magnitude of the

friction angle ϕ. For all cases, the model outcome converges at approximately 10,000 elements. This suggests that convergence is not governed by the model parameters of the soil, but is instead primarily dependent on the geometry of the model.

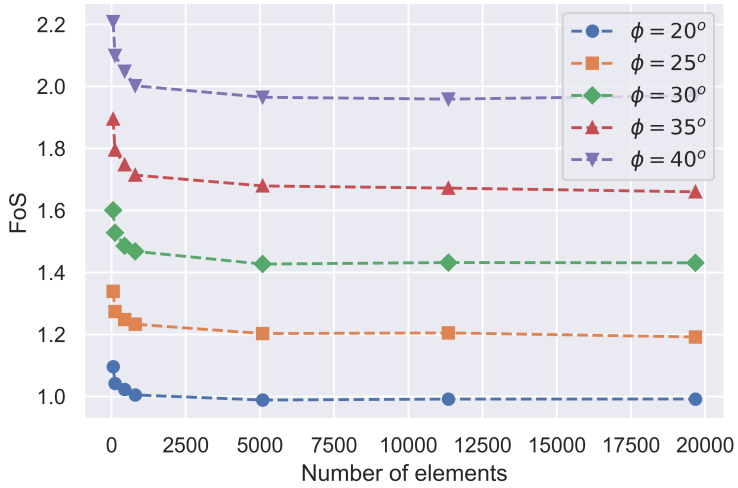

Figure 37: Effect of mesh refinement on model outcome in terms of FoS for varying friction angle ϕ in the case of $\psi = 0°$

In addition to evaluating the model outcome, the simulated failure mechanism is assessed under mesh refinement. More specifically, attention is given to the formation of the shear band. Figure 38 presents the development of shear bands for increasing mesh densities in the case of $\psi = \phi$. In this case, both the shape and thickness of the shear band remain relatively consistent under mesh refinement, indicating limited sensitivity to mesh refinement. Note that the mesh containing 11,350 elements, depicted in Figure 38c, was applied in Chapter 3.

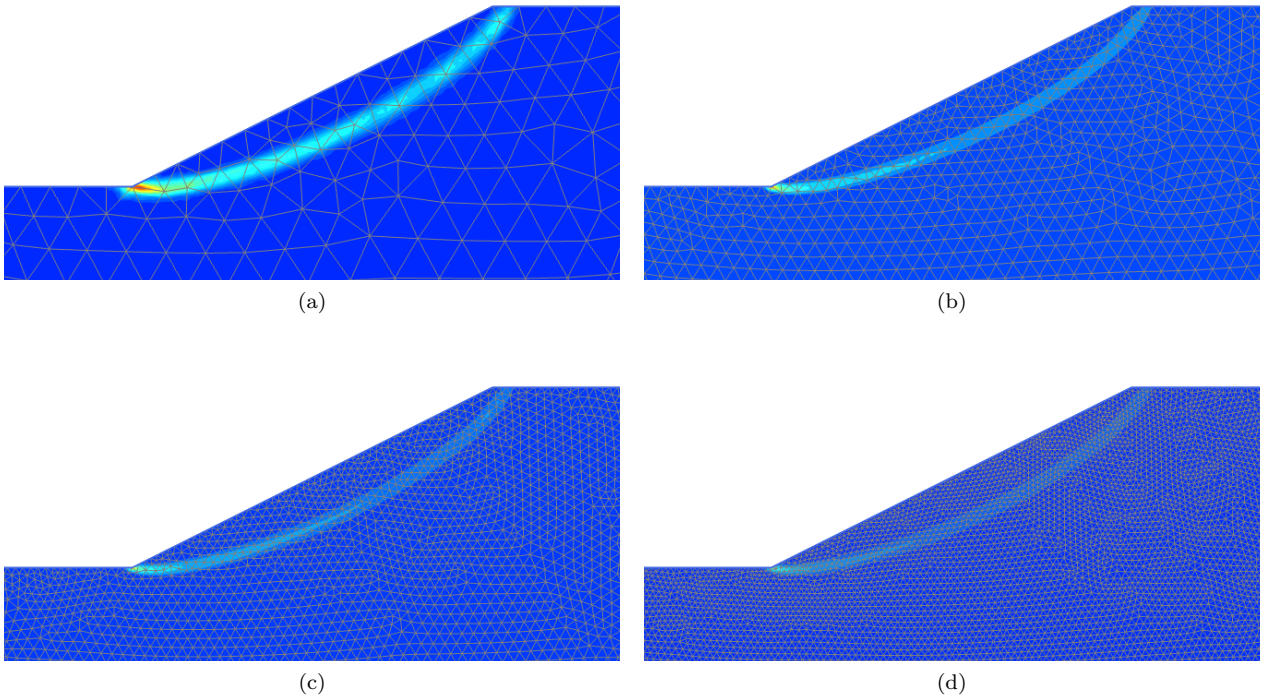

Figure 38: Shear band formation in the slope stability simulation for the case of $\psi = \phi$ using a mesh of: (a) 796 elements; (b) 5,093 elements; (c) 11,350 elements; (d) 28,902 elements

The shear bands for the case of $\psi = 0°$ with increasing mesh density are illustrated in Figure 39. It is evident that mesh refinement has a significant influence on the thickness of the formed shear band. The thickness of the shear band decreases significantly with mesh refinement. This behavior is a consequence of the absence of an internal length scale in the model to constrain shear band thickness. Since non-associated plasticity is used in this case, the model will show strain localization. As a result, the formed shear band will thin indefinitely with further mesh refinement and theoretically approaches a zero-thickness shear band (Mühlhaus and Vardoulakis, 1987). In reality, a shear band has a finite thickness, amounting to a small multiple of the mean grain diameter. This finite width is due to the microstructural interaction between the soil particles, such as grain rotation and contact forces (Desrues et al., 1996).

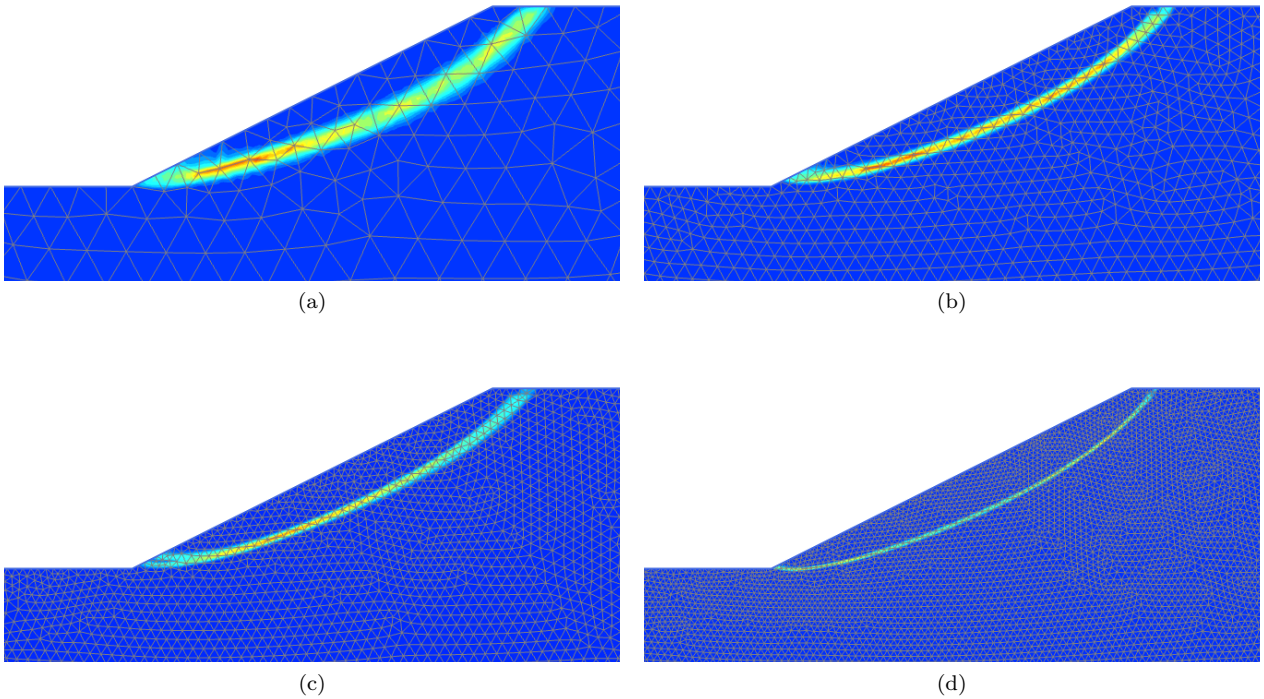

(a) (b) (c) (d)

Figure 39: Shear band formation in the slope stability simulation for the case of $\psi = 0°$ using a mesh of: (a) 796 elements; (b) 5,093 elements; (c) 11,350 elements; (d) 28,902 elements

In summary, the results show that in the case of $\psi = \phi$ the model outcome of a slope stability problem is relatively insensitive to mesh refinement. The model outcome proved to be stable even at moderate mesh densities. Correspondingly, the shape and thickness of the shear bands remain consistent as mesh densities increase. In contrast, the model outcome corresponding to the case of $\psi = 0°$ showed to be strongly mesh dependent. The FoS decreased by 8.5% with mesh refinement, showing a variation of approximately 1.4% post-convergence, which was reached at around 8,000 elements. Moreover, the thickness of the shear bands decreased substantially with mesh refinement. This behavior is a consequence of the absence of an internal length scale in the model, allowing the shear band to thin indefinitely, theoretically approaching zero thickness with further refinement. Furthermore, the analysis demonstrated that the mesh density required for convergence is largely dependent on geometry applied in the model. These findings highlight the importance of the applied mesh density in FEM, especially when using non-associated plasticity ($\psi = 0°$), to ensure reliable model outcome.

4.2 Retaining structure

This section investigates the influence of mesh refinement on the model outcome of the retaining structure problem previously introduced in Chapter 3.2. The analysis will be done for both the case of $\psi = \phi$ and $\psi = 0°$. For this problem, the primary focus is on the bending moment distribution within the retaining structure as the key model outcome. In addition, the simulated failure mechanism, particularly the development of

shear bands in the surrounding soil, is evaluated under different mesh densities. The geometry of the retaining structure model is illustrated in Figure 25. The corresponding soil and structural properties are listed in Table 6 and 7 respectively.

The degree of mesh refinement is illustrated in Figure 40. Figure 40a shows the coarsest mesh, consisting of 213 elements, and Figure 40b shows the finest mesh, consisting of 47,743 elements. It is important to note that in PLAXIS automatically applies local mesh refinement around a structural element, to better capture stress concentration and interaction effects.

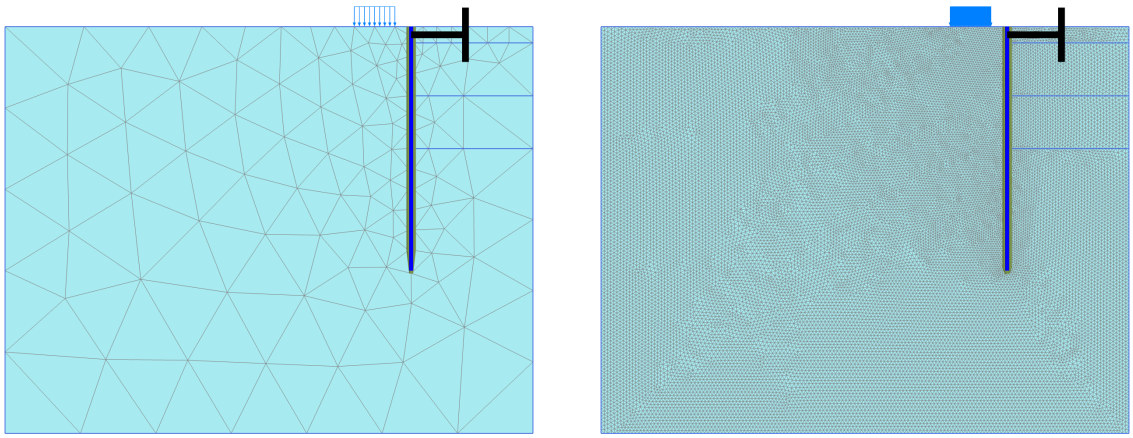

(a) (b)

Figure 40: Degree of mesh refinement applied in the retaining structure model: (a) Coarsest mesh consisting of 213 elements; (b) Finest mesh consisting of 47,743 elements

The effect of mesh refinement on the model outcome, in terms of bending moment, of the retaining structure simulation is illustrated in Figure 41. In this figure, the solid lines represent the bending moment obtained with the coarsest mesh. The dotted lines represent the bending moment obtained with a finer mesh. A trend similar trend to that of the slope stability analysis can be observed. In the case of $\psi = \phi$, the bending moment on the retaining structure is relatively independent to mesh density. In contrast, the bending moment in the case of $\psi = 0°$ shows strong dependence on the mesh refinement. Similar to the slope stability simulations, this analysis proved that when using non-associated plasticity coarser meshes tend to yield more conservative soil strength. Finer meshes simulate lower mobilize strength due to increase strain localization, which in turn leads to a higher bending moment on the retaining structure.

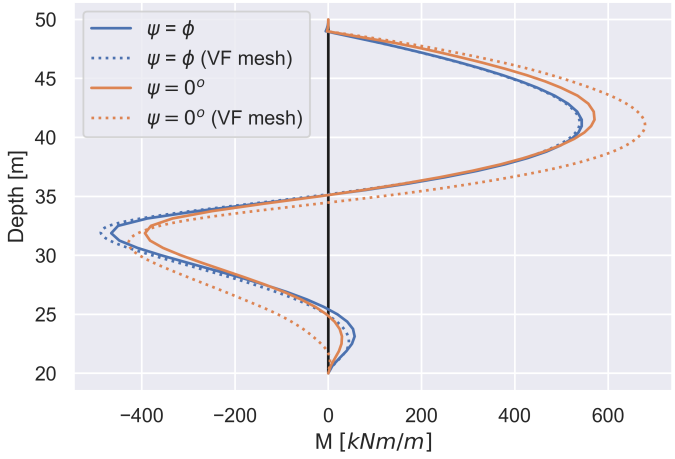

Figure 41: Effect of mesh refinement on model outcome in terms of bending moment acting on the retaining structure for the case of $\psi = \phi$ and $\psi = 0°$

As discussed in Chapter 3, the two cases result in different failure mechanisms, which in turn influence the strain development and consequently the stress change in the simulation. For the case of $\psi = \phi$, the bending moment is largely insensitive to mesh refinement. Only a slight increase in the negative bending moment is observed with mesh refinement. The behavior is a result of the failure mechanism developing at the passive side of the retaining structure, where the wall pushes against the soil. In this region the soil tends to dilate heavily, however its deformation is constrained. Mesh refinement allows this failure mechanism to be more accurately captured, leading to localized increase in bending moment. In contrast, the case of $\psi = 0°$ shows strong sensitivity to mesh refinement. Both the positive and negative bending moment increase significantly as the mesh is refined. The difference in positive and negative bending moment between coarsest and finest mesh in this case reaches approximately 19% and 9% respectively. This result reflects the influence of strain localization associated with non-associated flow, which becomes more pronounced with finer mesh densities.

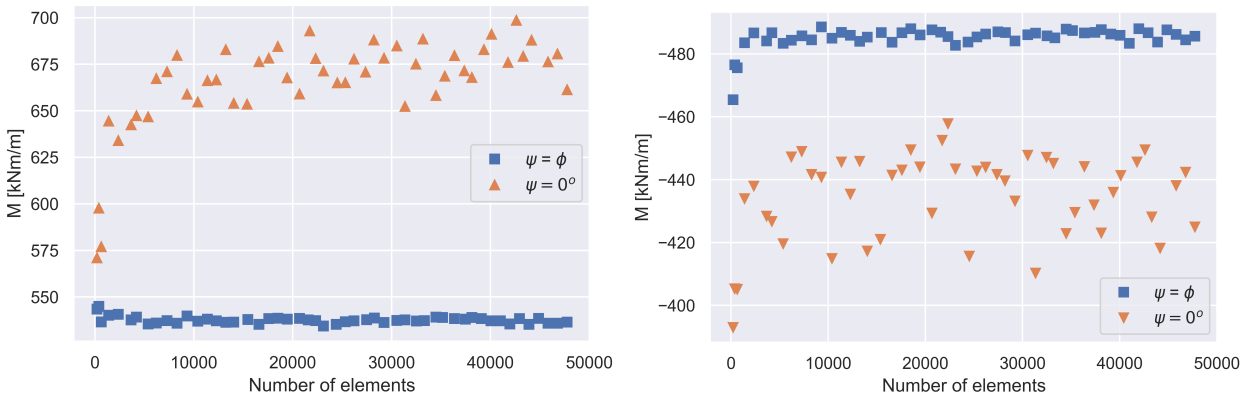

(a) (b)

Figure 42: Effect of mesh refinement on model outcome acting on the retaining structure for the case of $\psi = \phi$ and $\psi = 0°$ in terms of: (a) Positive bending moment; (b) Negative bending moment

The convergence of the model outcome, in terms of positive and negative bending moment, is illustrated in Figure 42. As with the slope stability simulations, the retaining structure analysis shows strong mesh dependence in the case of $\psi = 0°$, while the case of $\psi = \phi$ shows relatively stable results with mesh refinement. Focusing on the convergence of the positive bending moment in the case of $\psi = 0°$, as shown in Figure 42a, a greater spread can be observed compared to the slope stability simulations. This variability is even more pronounced in the negative bending moment, illustrated in Figure 42b. The observed scatter is a result of the formation of shear bands. The shear strain plots (Figure 45) reveal that the location and intensity of shear bands in the retaining structure varies across different mesh densities, particularly near the base of the retaining wall. These localized strain concentrations influence the internal forces within the wall, including the bending moment. This explains the greater scatter observed in the convergence plots, highlighting the increased sensitivity to mesh refinement in problems where soil deformation is constrained, such as retaining structures.

The model outcome corresponding to the "very fine" mesh preset in PLAXIS is highlighted in Figure 43. In this geometry the "very fine" mesh preset contains 2,361 elements. As with previous results, the "very fine" mesh proves to be sufficiently refined for the case of $\psi = \phi$, as the bending moment output remains unchanged with further mesh refinement. However, in the case of $\psi = 0°$ required further mesh refinement for convergence. This once again proved that the "very fine" mesh preset is not adequate when using non-associated plasticity due to the model's increased sensitivity to strain localization and mesh density.

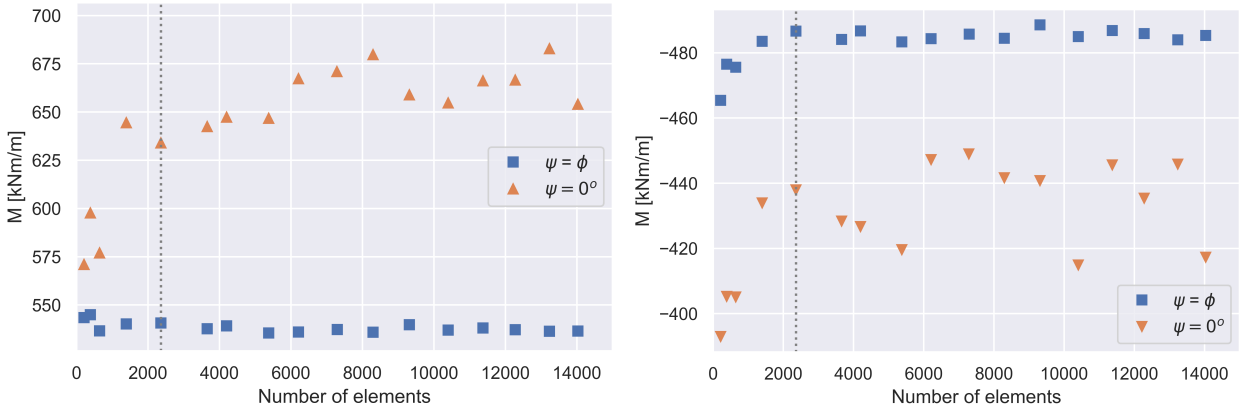

(a) (b)

Figure 43: Highlighted model outcome of the retaining structure simulation for the "very fine" mesh preset in PLAXIS for the case of $\psi = \phi$ and $\psi = 0°$ in terms of: (a) Positive bending moment; (b) Negative bending moment

As highlighted in the previous chapter, the case of $\psi = \phi$ does not show pronounced shear banding in the shear strain plots. Therefore, to evaluate the influence of the mesh refinement on the simulated failure mechanism, incremental displacement plots are assessed instead. These are illustrated in Figure 44. As shown, the displacement patterns remain consistent with increasing mesh density, further confirming the mesh independent behavior of the associated plasticity formulation in this retaining structure simulation.

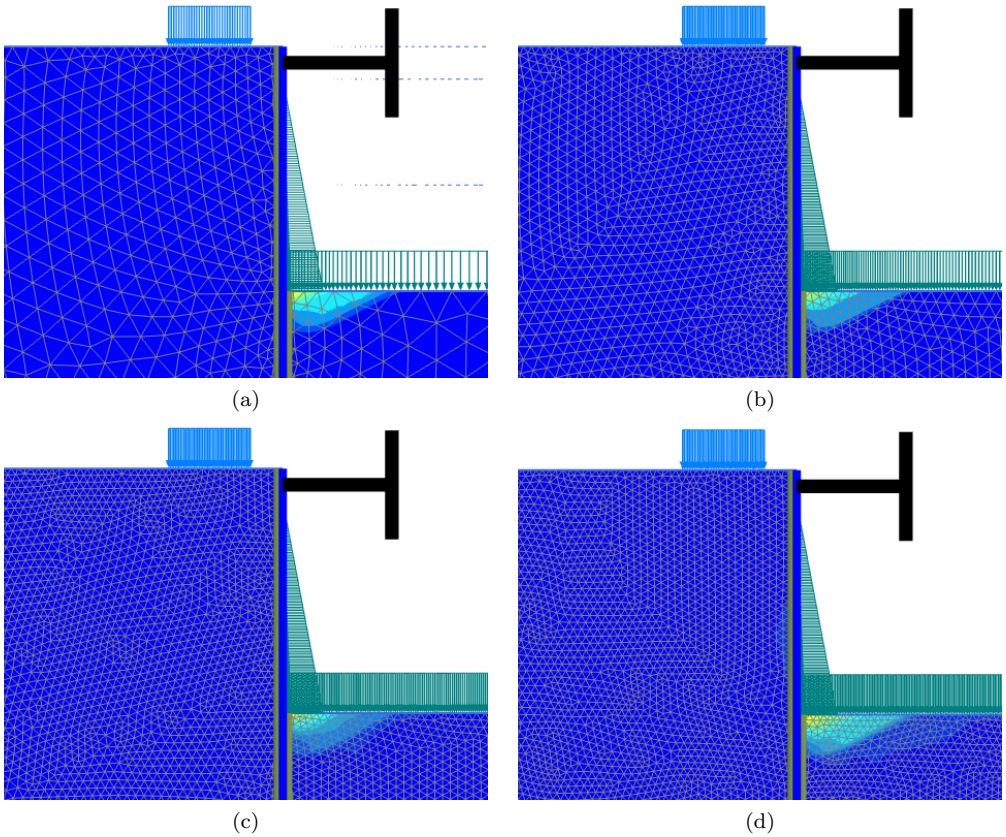

(a) (b)

(c) (d)

Figure 44: Total incremental displacement in the retaining structure simulation for the case of $\psi = \phi$ using a mesh of: (a) 2,361 elements; (b) 11,403 elements; (c) 26,204 elements; (d) 35,478 elements

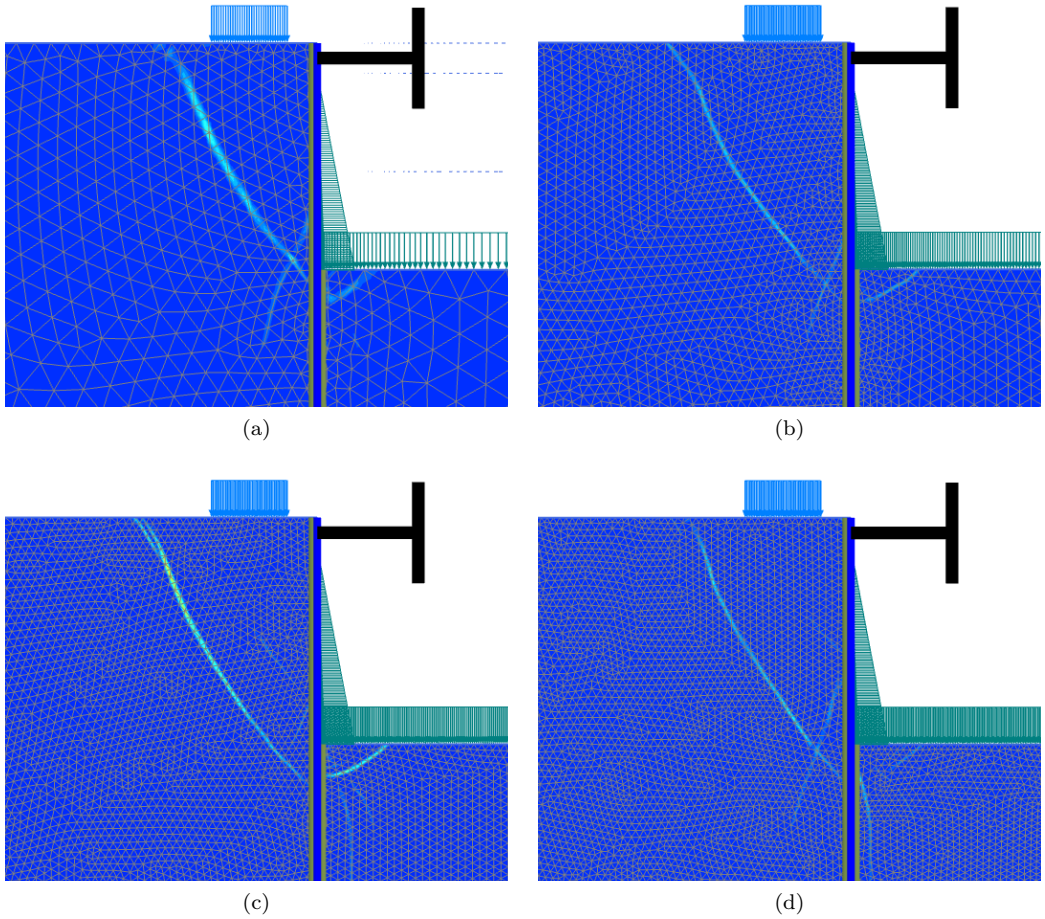

Figure 45: Shear band formation in the retaining structure simulation for the case of $\psi = 0°$ using a mesh of: (a) 2,361 elements; (b) 11,403 elements; (c) 26,204 elements; (d) 35,478 elements

The shear band formation with increasing mesh refinement for the case of $\psi = 0°$ is illustrated in Figure 45. As observed in the slope stability simulations, the shear bands become progressively thinner with finer mesh densities, due to the model lacking an internal length scale. Additionally, the intensity of the shear strain, indicated by the shaded lines, also increases with mesh refinement. Particularly the shear bands near the lower part of the retaining wall vary in location and intensity across mesh densities. This variability introduces considerable uncertainty in the bending moment along the retaining structure. The inconsistency in strain localization patterns at the lower part of the structure explains the considerable spread observed in the convergence plots, particularly for the negative bending moment.

This section examined the influence of mesh refinement on the numerical behavior of the retaining structure, for both cases of $\psi = \phi$ and $\psi = 0°$. The primary focus was on the bending moment distribution along the retaining structure, with additional evaluation of failure mechanisms through displacement and shear strain plots. The results demonstrate that the case of $\psi = \phi$ produces mesh independent results. Both bending moments and displacement patterns remained consistent across different mesh densities, and shear banding was not strongly expressed. In contrast, the case of $\psi = 0°$ showed clear dependence on mesh density, with the bending moment starting to converge after approximately 11,000 elements, though it continued to show a wide scatter across different mesh densities. The bending moment, especially the negative component, showed significant variation with mesh refinement. Shear strain plots revealed increasingly narrow and intense shear bands with refinement, particularly near the base of the wall.

5 Equivalent associated plasticity

While non-associated plasticity models offer a more accurate representation of granular soil behavior, they are often accompanied by numerical challenges. These include mesh dependence, localization and non-unique solutions in FEM simulations. To address these limitations, equivalent associated plasticity approaches have been proposed. These methods simulate non-associated behavior by adjusting strength parameters within an associated flow rule framework, offering improved numerical robustness. This chapter explores the effectiveness of equivalent associated plasticity, with particular focus on the approach proposed by Davis (1968). The method is evaluated using the same three problems introduced in previous chapters: the DSS test, the slope stability model and the retaining structure model. The objective is to assess to what extent equivalent associated models can replicate the mechanical response of non-associated models and to identify the limitations and conditions under which they provide a reliable approximation.

5.1 DSS test simulation

To validate the applicability of equivalent associated plasticity a DSS test is simulated in PLAXIS SoilTest. The simulation setup mirrors the earlier case described in Chapter 3, ensuring a consistent basis for comparison. The material parameters applied are listed in Table 8. In this case, an equivalent associated model is established by calculating an equivalent friction angle ϕ_{EQV} based on the Davis approach (Equation 18). This equivalent friction angle is then used in an associated flow rule framework by setting the dilatancy angle $\psi = \phi_{EQV}$. This allows for simulating non-associated behavior within an associated plasticity model, thereby improving numerical stability.

Table 8: Material parameters used for the equivalent associated sample in the DSS test simulation

Description	Symbol	Value
Unsaturated unit weight	γ_{unsat}	0 kN/m^2
Saturated unit weight	γ_{sat}	0 kN/m^2
Young's modulus	E'_{ref}	10,000 kN/m^2
Poisson's ratio	ν	0.3
Consolidation	K_0	0.5
Cohesion	c'_{ref}	0 kN/m^2

Using the material properties listed in Table 8, a DSS test is simulated in PLAXIS SoilTest to evaluate the performance of the equivalent associated plasticity model in replicating shear strength. The equivalent friction angle ϕ_{EQV} is calculated using Equation 18, with $\phi = 30°$ and $\psi = 0°$ as input. The corresponding parameter sets for both cases are provided in Table 9. The results are presented in Figure 46, which illustrates the shear stress–shear strain relations for the two cases of $\psi = 0°$ and $\psi = \phi_{\mathrm{EQV}}$.

Table 9: Parameter sets applied in the DSS simulation

Parameter	Non-associated flow ($\psi = 0°$)	Equivalent associated flow ($\psi = \phi_{EQV}$)
Friction angle	$\phi = 30°$	$\phi = 26.6°$
Dilatancy angle	$\psi = 0°$	$\psi = 26.6°$

The simulated mobilized shear stress is identical for the cases of $\psi = \phi_{EQV}$ and $\psi = 0°$. As explained in Chapter 3, a non-associated case will show mobilized strength as defined by the Davis approach for non-dilatant material (Equation 15). With an initial vertical stress σ_{yy} of $100kN/m^2$ and a friction angle of $30°$ in the case of $\psi = 0°$ will lead to a mobilized shear strength of $\tau = 100kN/m^2 \cdot \sin(30°) = 50kN/m^2$. An associated case will follow the classical Coulomb equation. In the case of $\psi = \phi_{EQV}$ this will yield a mobilized shear strength of $\tau = 100kN/m^2 \cdot \tan(26.6°) = 50kN/m^2$. This confirms that the equivalent associated plasticity approach reproduces the same mobilized shear strength as the non-associated model. The mobilized shear strength is illustrated in Figure 46 for both cases.

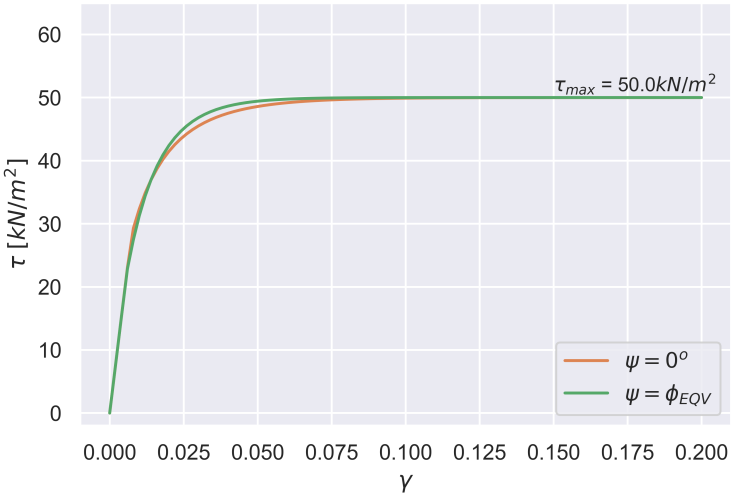

Figure 46: Shear stress - shear strain relation from a DSS simulation for non-associated plasticity ($\psi = 0°; \phi = 30°$) and equivalent plasticity ($\psi = \phi_{EQV} = 26.6°$)

The corresponding stress paths for the DSS simulation presented in Figure 46 are illustrated in Figure 47. In the case of $\psi = \phi_{EQV}$, more plastic strain is simulated due to the higher dilatancy angle. As discussed earlier, the magnitude of plastic strain generated is primarily governed by the value of ψ. Additionally, it can be observed that the stress path in the case of $\psi = \phi_{EQV}$ follows a different failure envelope than the case of $\psi = 0°$. This is a result of the difference in friction angle, as the cases where simulated for $\phi_{EQV} = 26.57°$ and $\phi = 30°$. Since the Mohr-Coulomb contour is directly influenced by the friction angle ϕ, each stress path will conform to its respective failure envelope. As a result, the stress evolution and failure mechanism differ slightly between the two models.

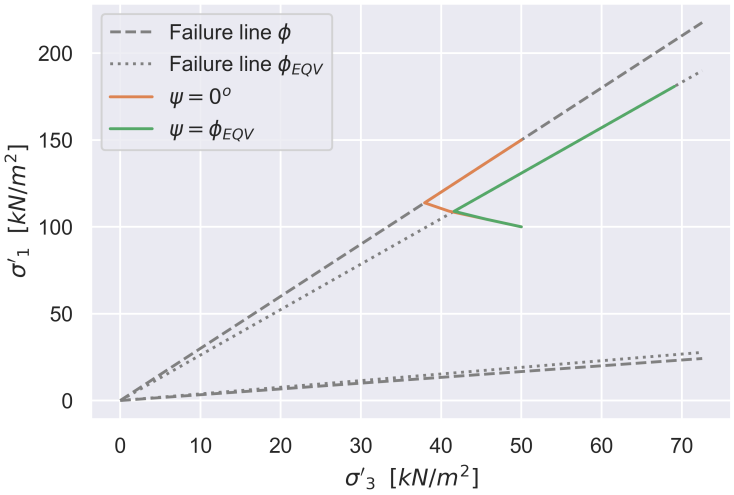

Figure 47: Stress path from a DSS simulation for non-associated plasticity ($\psi = 0°; \phi = 30°$) and equivalent plasticity ($\psi = \phi_{EQV} = 26.6°$) with corresponding failure lines

In Figure 48 the Mohr's circles corresponding to the final stress state are illustrated, for both the cases of $\psi = 0°$ and $\psi = \phi_{EQV}$. Although both simulations exhibit the same mobilized shear strength, the maximum shear strength in the final stress state, defined as $\tau = \frac{\sigma_1 - \sigma_3}{2}$, differs between the two cases. For the case of $\psi = 0°$ with $\sigma_1 = 150kN/m^2$ and $\sigma_3 = 50kN/m^2$, the maximum shear strength is $\tau = 50kN/m^2$. In contrast, the case of $\psi = \phi_{EQV}$ yields $\sigma_1 = 180kN/m^2$ and $\sigma_3 = 70kN/m^2$, resulting in a maximum shear strength is

$\tau = 55kN/m^2$. This discrepancy arises from the use of an associated flow rule in the equivalent model, which permits greater plastic volumetric deformation, thereby altering the stress redistribution despite achieving the same mobilized shear strength.

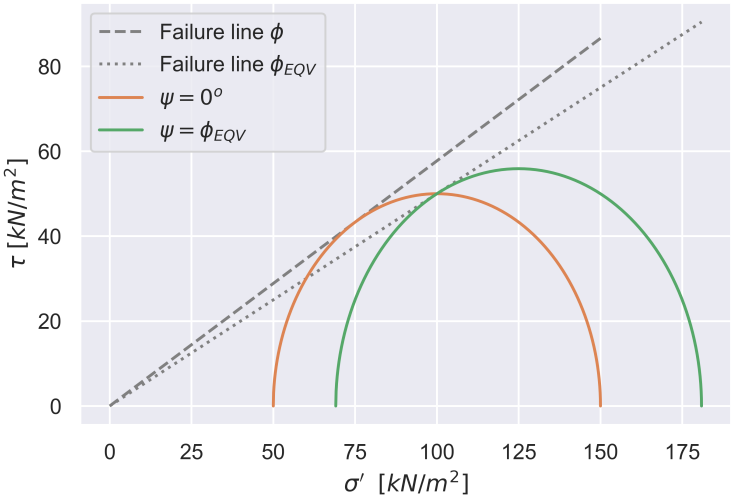

Figure 48: Mohr circles for the DSS simulation for non-associated plasticity ($\psi = 0°; \phi = 30°$) and equivalent plasticity ($\psi = \phi_{EQV} = 26.6°$) with corresponding failure lines

In this section, a DSS test was simulated using PLAXIS SoilTest to evaluate the effectiveness of equivalent associated plasticity in replicating non-associated behavior. Two cases were compared: a non-associated model with $\psi = 0°$ and $\phi = 30°$, and an equivalent associated model using $\psi = \phi_{EQV} = 26.6°$. Both simulations yielded the same mobilized shear strength of $50kN/m^2$, validating that equivalent associated plasticity can accurately reproduce the strength behavior of a non-dilatant material. However, differences were observed in plastic strain development and stress path trajectories. The equivalent associated model, due to its non-zero dilatancy angle, showed more plastic deformation and followed a different Mohr-Coulomb contour. Mohr's circle analysis further revealed that while the mobilized shear strength was identical, the maximum shear strength differed between the two cases due to differing flow rule. These findings confirm that equivalent associated plasticity can replicate the strength of non-associated behavior, but introduces differences in deformation characteristics due to the associated flow rule framework.

5.2 Slope stability

In the DSS simulation, the equivalent associated plasticity, based on the Davis approach, was shown to accurately reproduce the mobilized shear strength of a non-associated model at a single stress point. However, slope stability analyses involve complex stress states and strain distributions. In this section, the performance of the equivalent associated plasticity is assessed in a slope stability model. The same slope geometry and material properties as presented in previous chapters are used to ensure consistency and comparability. The parameter sets applied for the associated and non-associated cases, along with the equivalent associated model, are listed in Table 10.

Table 10: Parameter sets applied to the slope stability model

Parameter	Associated flow ($\psi = \phi$)	Non-associated flow ($\psi = 0°$)	Equivalent associated flow ($\psi = \phi_{EQV}$)
Friction angle	$\phi = 30°$	$\phi = 30°$	$\phi = 26.6°$
Dilatancy angle	$\psi = 30°$	$\psi = 0°$	$\psi = 26.6°$

The relation between mesh size and the FoS is illustrated in Figure 49 for three cases: associated ($\psi = \phi$), non-associated ($\psi = 0°$) and equivalent associated ($\psi = \phi_{EQV}$). As expected, the model outcome for the case of $\psi = \phi_{EQV}$ shows limited sensitivity to mesh refinement, attributed to the use of an associated flow

rule. However, the FoS predicted by this case is significantly lower than that of the case of $\psi = 0°$ on which the equivalent model was based. This indicates that the equivalent associated plasticity simulates a weaker soil response than the original non-associated model. This underprediction is a direct result of the conservative nature of the Davis approach. As discussed in the literature review, the Davis method provides a lower boundary of shear strength by assuming the orientation of the shear band follows $\beta = 45° + \frac{\psi}{2}$, with $\psi = 0°$ in the non-dilatant case. In contrast, the upper boundary corresponds to $\beta = 45° + \frac{\phi}{2}$, which results in the classical Coulomb relation. The true failure mechanism likely lies somewhere between these bounds. Therefore, while the Davis approach offers a simplified and robust means to approximate non-associated behavior within an associated framework, it inherently yields conservative predictions in boundary value problems such as slope stability.

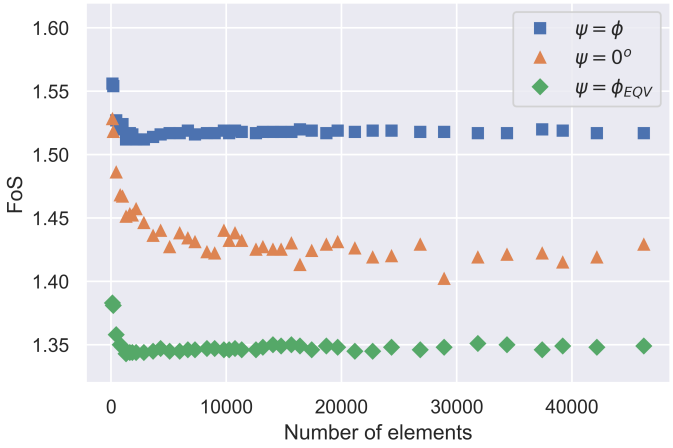

Figure 49: Effect of mesh refinement on model outcome in terms of FoS for the slope stability simulation in the case of $\psi = \phi$, $\psi = 0°$ and $\psi = \phi_{EQV}$

Figure 50 presents the model outcome corresponding to the "very fine" mesh preset in PLAXIS for the three cases. It can be observed that the "very fine" mesh is sufficiently refined for the case of $\psi = \phi_{EQV}$, as the FoS stabilizes and becomes nearly mesh independent. This indicates that the equivalent associated plasticity model performs well in terms of numerical stability and convergence. Despite its conservative prediction of shear strength, as discussed previously, the method shows promise in producing consistent and mesh independent results. This characteristic is particularly valuable in practical applications, where mesh sensitivity can compromise the reliability of FEM simulations.

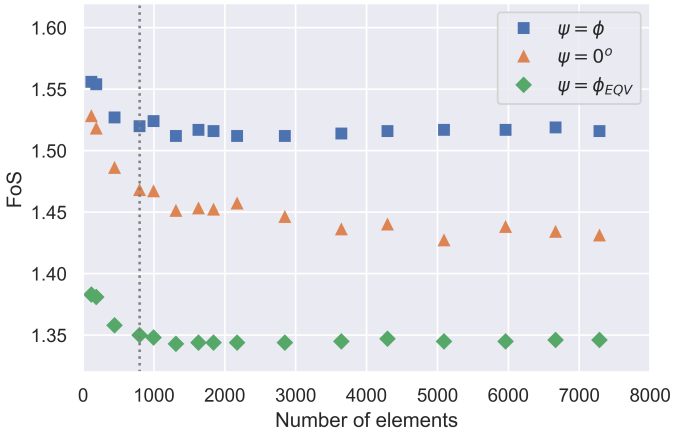

Figure 50: Highlighted model outcome of the slope stability simulation for the "very fine" mesh preset in PLAXIS for the case of $\psi = \phi$, $\psi = 0°$ and $\psi = \phi_{EQV}$

By reducing the friction angle from 30° to 27.8°, referred to as ϕ_{RED}, the model outcome from the non-associated case with $\psi = 0°$ was successfully matched. Since this reduced friction angle was applied within an associated plasticity framework, the model was not strongly mesh dependent. This demonstrates that an associated model with a carefully calibrated reduced friction angle can replicate the behavior of a non-associated model, while avoiding the numerical issues typically experienced with non-associated formulations. Notably, the reduced friction angle ϕ_{RED} is approximately 0.9 times the actual friction angle, which could a practical rule of thumb for calibrating equivalent associated models. Furthermore, the value of ϕ_{RED} falls between the actual friction angle and the equivalent friction angle ($\phi_{EQV} < \phi_{RED} < \phi$), confirming that the true simulated mobilized strength lies between the upper and lower bounds defined by the Coulomb and Davis formulations respectively.

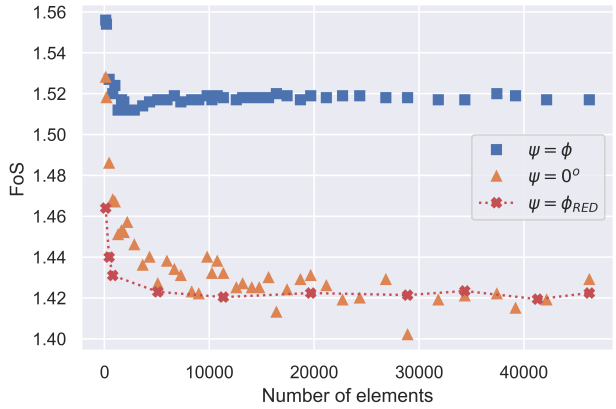

Figure 51: Effect of mesh refinement on model outcome in terms of FoS for the slope stability simulation in the case of $\psi = \phi$, $\psi = 0°$ and $\psi = \phi_{RED}$

Figure 52 illustrated the shear band formation of the slope stability simulations for the cases of non-associated plasticity ($\psi = 0°$), associated plasticity ($\psi = \phi$), equivalent associated plasticity ($\psi = \phi_{EQV}$) and reduced associated plasticity ($\psi = \phi_{RED}$). The failure mechanisms appear highly similar across all associated cases. This indicates that in this relatively unconstrained problem, the equivalent associated models do not significantly influence the development of the shear band.

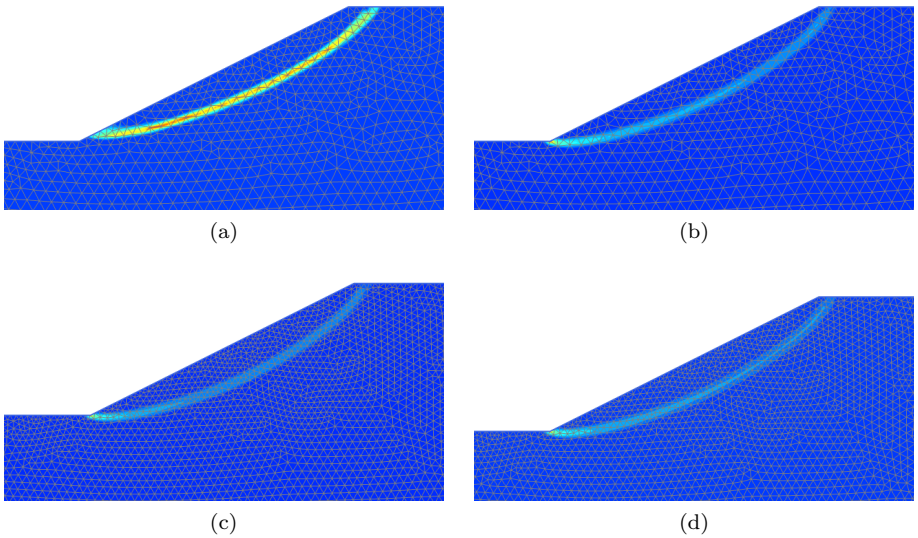

Figure 52: Shear strain plot showing the shear band formation of the slope stability simulation for the case of: (a) $\psi = 0°$ & $\phi = 30°$; (b) $\psi = \phi = 30°$; (c) $\psi = \phi_{EQV} = 26.6°$; (d) $\psi = \phi_{RED} = 27.8°$

To summarize, the slope stability simulations evaluated the performance of equivalent associated plasticity ($\psi = \phi_{EQV}$) in a boundary value problem. While ϕ_{EQV}, derived using the Davis approach, matched the mobilized shear strength of a non-associated model in a DSS test simulation, its application in slope stability revealed key limitations. Specifically, the case of $\psi = \phi_{EQV}$ yielded mesh independent results, a major benefit of the associated flow rule. However, the FoS was significantly lower than the reference non-associated case ($\psi = 0°$), indicating that the Davis approach yields conservative model outcome. This conservatism arises from the Davis assumption of a shear band orientation of $\beta = 45° + \frac{\psi}{2}$ for $\psi = 0°$, which represents a lower bound for strength. To improve accuracy, a reduced friction angle $\phi_{RED} = 27.8°$ (approximately $0.9\,\phi$) was calibrated and used in an associated model. This adjustment produced FoS results that closely matched the non-associated case, without the mesh sensitivity issues. This confirms that with proper calibration, equivalent associated models can be practical alternatives for slope stability problems, provided that strength bounds are interpreted carefully.

5.3 Retaining structure

The equivalent associated plasticity model is further tested and validated using a retaining structure simulation. Unlike slope stability problems, retaining structures impose significant restriction on the soil's ability to deform freely. As highlighted in earlier chapters, this constraint amplifies the differences between associated and non-associated plasticity formulations. This section assesses the applicability of an equivalent associated model in such a setting using PLAXIS 2D. The necessary conditions and limitations for accurate modeling with this approach are discussed in detail. To ensure consistency and comparability the same geometry, soil and structural properties as presented in previous chapters are used. The parameter sets applied for the associated, non-associated, and equivalent associated cases are listed in Table 11.

Table 11: Parameter sets applied to the retaining structure model

Parameter	Associated flow ($\psi = \phi$)	Non-associated flow ($\psi = 0°$)	Equivalent associated flow ($\psi = \phi_{EQV}$)
Friction angle	$\phi = 35°$	$\phi = 35°$	$\phi = 29.8°$
Dilatancy angle	$\psi = 35°$	$\psi = 0°$	$\psi = 29.8°$

The relation between mesh size and the bending moment is illustrated in Figure 53 for three cases: associated flow ($\psi = \phi$), non-associated flow ($\psi = 0°$), and the equivalent associated model ($\psi = \phi_{EQV}$). As expected, the case of $\psi = \phi_{EQV}$ shows limited sensitivity to mesh refinement, which can be attributed to the use of an associated plasticity formulation. However, the predicted bending moments, both positive and negative, are significantly increased in the equivalent model. This increase can be attributed to two main factors. First, the equivalent model simulates a lower soil strength due to the conservative nature of the Davis approach. As a result, the soil carries less of the applied load, which leads to the retaining structure taking on more load, thereby increasing the positive bending moment on the active side. Second, the negative bending moment is also elevated, which is a result of a different failure mechanism. Because the equivalent model uses $\psi = \phi_{EQV}$ in an associated framework, the soil tends to dilate significantly upon loading. This dilation is constrained by the retaining structure, leading to increased stress that increase the bending moment on the passive side.

The same trend as with the slope stability model is observed in the case of the retaining structure model. The equivalent friction angle ϕ_{EQV} does not yield the same results as the case of $\psi = 0°$. In the slope stability model the equivalent friction angle proved to simulate a weaker ground yielding a lower FoS. In the retaining structure problem the equivalent friction angle also yielded a weaker soil yielding a higher bending moment on the retaining structure. Figure 53 illustrated the maximum and minimum bending moment acting on the retaining structure. The equivalent model shows to be not strongly mesh dependent as it is used as an associated case.

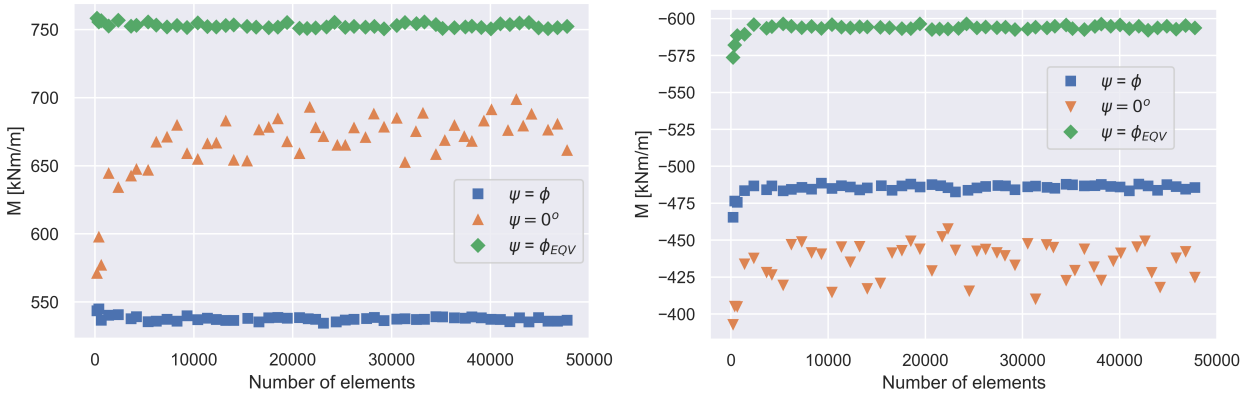

Figure 53: Effect of mesh refinement on model outcome acting on the retaining structure for the case of $\psi = \phi$, $\psi = 0°$ and $\psi = \phi_{EQV}$ in terms of: (a) Positive bending moment; (b) Negative bending moment

In Figure 54, the bending moment distribution along the length of the retaining structure is illustrated. The figure demonstrates that both the positive and negative bending moments are increased in the equivalent associated plasticity model. This increase is attributed to two main factors. The lower simulated soil strength, which causes the retaining structure to carry a larger portion of the load increasing the positive bending moment. The modified failure mechanism resulting from the associated flow assumption enhancing volumetric expansion and leads to higher negative bending moments near the excavation.

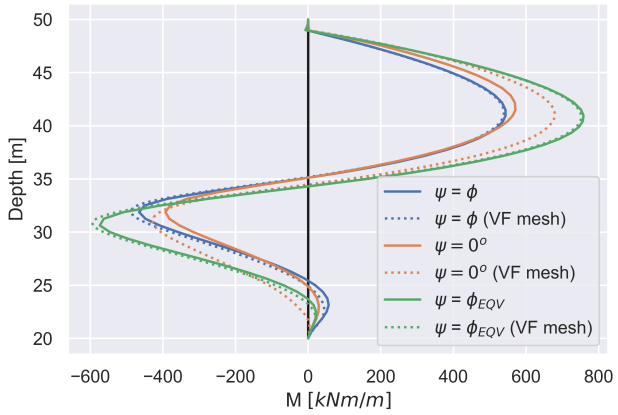

Figure 54: Bending moment distribution in the retaining structure for the cases of $\psi = \phi$, $\psi = 0°$, and $\psi = \phi_{EQV}$

The equivalent associated plasticity model based on the Davis approach again demonstrated poor performance in the retaining structure simulations. To address this, the friction angle was reduced to a value of 31.6° in order to match the model outcome of the non-dilatant non-associated case. Notably, this reduced friction angle corresponds to approximately 0.9 times the actual friction angle ($0.9\,\phi$), consistent with findings from the slope stability simulations. It is important to emphasize that only the positive bending moment could be accurately matched with this reduced friction angle. Due to the differing failure mechanisms between associated and non-associated models, the negative bending moment remains overestimated. In the equivalent and reduced associated plasticity cases, the failure mechanism becomes dominant on the passive side of the retaining structure, resulting in higher negative bending moments. Attempting to match the negative bending moment would require an unrealistically low friction angle, which would severely underestimate the positive bending moment. Furthermore, in practical design the positive bending moment, governed by the active side of the structure, is typically leading.

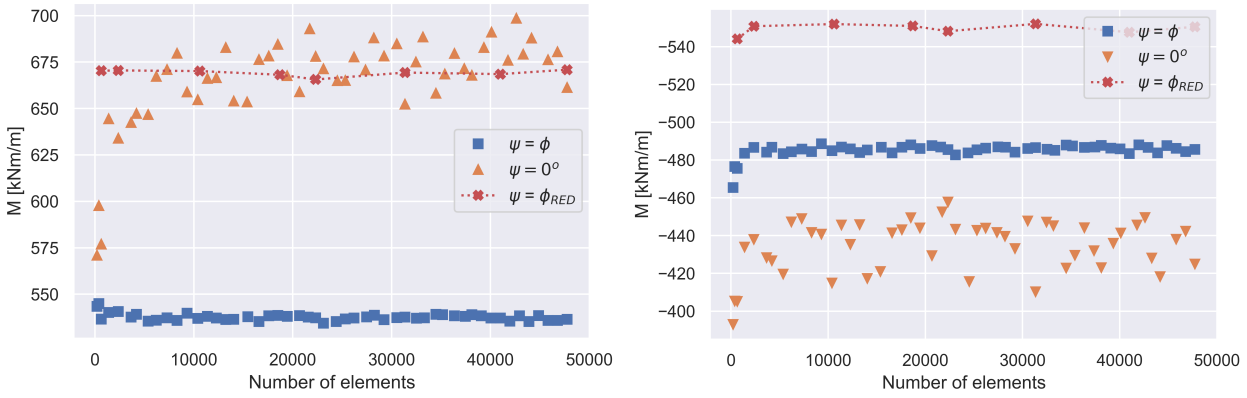

Figure 55: Effect of mesh refinement on model outcome acting on the retaining structure for the case of $\psi = \phi$, $\psi = 0°$ and $\psi = \phi_{RED}$ in terms of: (a) Positive bending moment; (b) Negative bending moment

In Figure 54, the bending moment distribution along the length of the retaining structure is illustrated for the reduced friction angle ϕ_{RED}. The figure shows that, compared to the non-associated model, the positive bending moment is successfully matched by reducing the friction angle to approximately 90% of its original value. This reduction compensates for the strength difference between the associated and non-associated models, allowing the soil to mobilize a comparable amount of resistance. However, the negative bending moment remains higher in the reduced friction angle model. This is due to the associated flow rule, which induces greater volumetric expansion and results in a different failure mechanism.

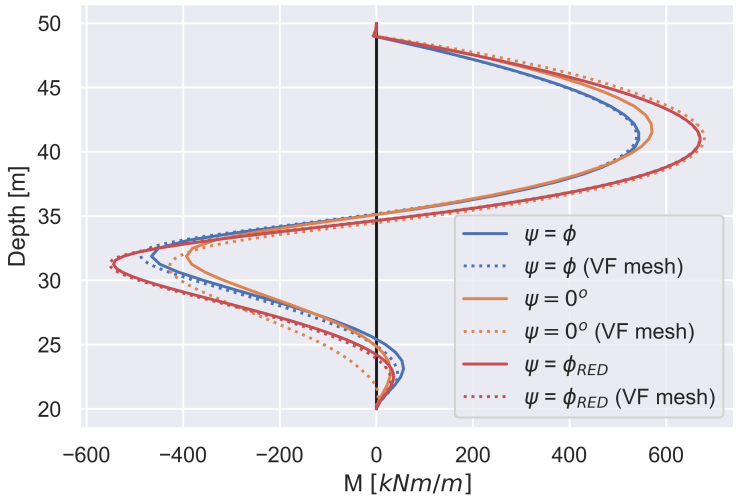

Figure 56: Bending moment distribution in the retaining structure for the cases of $\psi = \phi$, $\psi = 0°$, and $\psi = \phi_{RED}$

Figure 57 illustrates the formation of the shear bands in the retaining structure simulations for the cases of non-associated plasticity ($\psi = 0°$), associated plasticity ($\psi = \phi$), equivalent associated plasticity ($\psi = \phi_{EQV}$) and reduced associated plasticity ($\psi = \phi_{RED}$). As previously discussed, the failure mechanism differs significantly between the associated and non-associated cases, primarily due to the influence of the dilatancy angle ψ. Among the associated models, the failure mechanisms appear largely consistent. However, cases with a higher dilatancy angle, set equal to the friction angle $\psi = \phi$, show more pronounced and dominant shear banding at the passive side of the retaining structure.

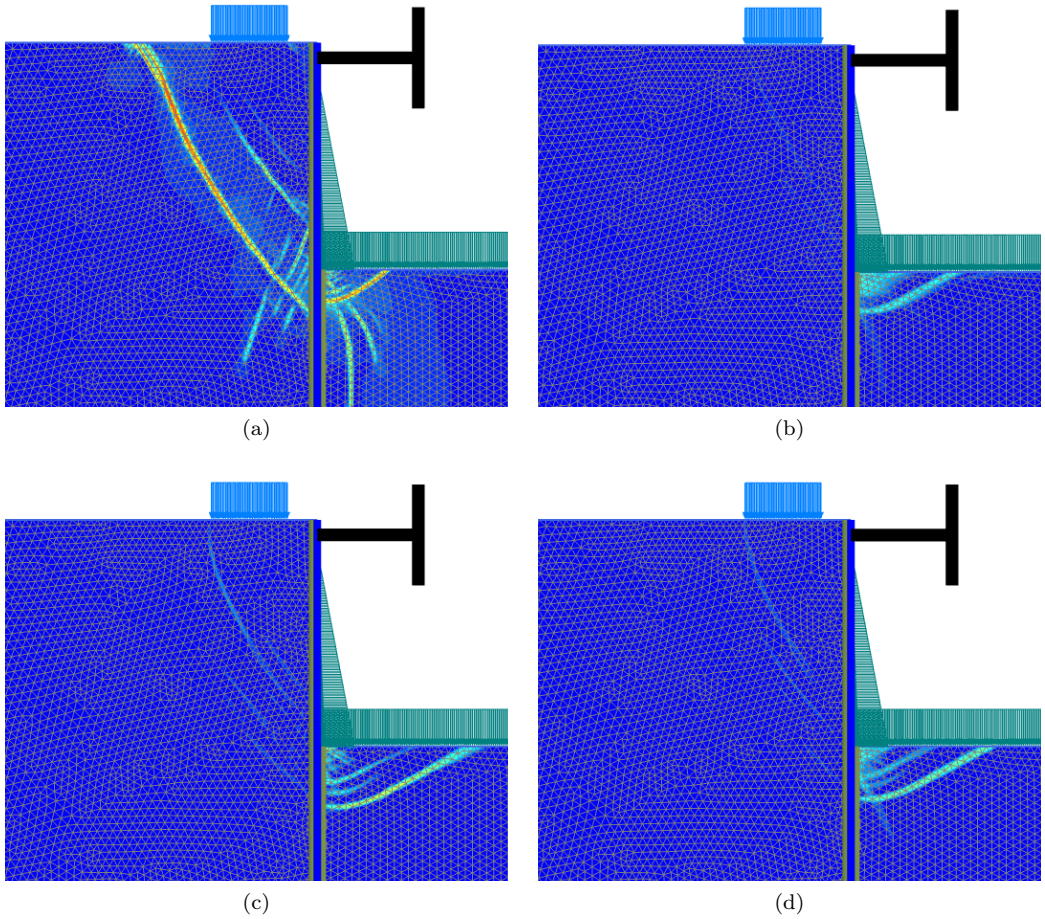

Figure 57: Shear strain plots on logarithmic scale showing the shear band formation of the retaining structure simulation for the case of: (a) $\psi = 0°$ & $\phi = 35°$; (b) $\psi = \phi = 35°$; (c) $\psi = \phi_{EQV} = 29.8°$; (d) $\psi = \phi_{RED} = 31.6°$

In this section, the applicability of equivalent associated plasticity was assessed using a retaining structure simulation. Compared to the slope stability problem, the retaining structure model involves more constrained deformation, which amplifies the difference between associated and non-associated plasticity. As expected, the equivalent associated model, based on the Davis approach, performed poorly in replicating the behavior of the non-associated case. The equivalent model significantly overestimated both the positive and negative bending moments. This was primarily due to two factors: (1) the underestimated soil strength in the equivalent model, causing the structure to carry more of the load, and (2) the different failure mechanisms resulting from using an associated flow rule, particularly the distinct local failure on the passive side. To improve the match, the friction angle was reduced to approximately 90% of the actual value ($\phi_{\mathrm{RED}} = 0.9\phi$), which allowed the positive bending moment to align with the non-associated case. However, the negative bending moment cannot be matched without reducing the friction angle to unrealistically low levels. Overall, while friction angle reduction can provide a partial correction, the equivalent associated model remains limited for accurately simulating non-associated behavior in retaining structures.

6 Conclusions & recommendations

This chapter presents the conclusions and recommendations based on the findings of this research. The aim of the study was to critically assess the assumptions and limitations of associated and non-associated plasticity in geotechnical FEM modeling, with a focus on the influence of the dilatancy angle ψ, mesh dependence, and the applicability of equivalent associated plasticity. Through a combination of literature review, direct simple shear (DSS) simulations, a slope stability model and a retaining structure model insight was gained into how these factors affect model outcome.

6.1 Conclusions

The conclusions are structured around the three research questions formulated at the start of this study. Each section summarizes the key findings that answer the corresponding question.

RQ1: "What is the influence of the dilatancy angle ψ, in relation to confined and constrained deformation, in the case of associated and non-associated plasticity?"

- DSS simulations demonstrated that the dilatancy angle ψ directly governs both mobilized shear strength and plastic strain development. The non-associated case ($\psi = 0°$) followed the Davis relation for non-dilatant material ($\sin\phi$), while the associated case ($\psi = \phi$) followed the Coulomb equation ($\tan\phi$), resulting in higher peak strength and plastic strain. Although the initial stress ratio K_0 did not affect the final stress state, it significantly influenced the stress path and plastic deformation. This is due to the dependence of the plastic potential function g on stress difference and ψ. As a non-isotropic initial stress condition is introduced (i.e. $K_0 \neq 1$), the stress difference becomes non-zero, increasing stress rotation and plastic strain. Overconsolidated, non-dilatant samples exhibited softening behavior, while associated cases did not. Mohr's circles shifted rightward with increasing ψ, indicating greater maximum strength while the failure envelope remained fixed.

- Slope stability simulations showed that the dilatancy angle ψ significantly affects the Factor of Safety (FoS). Non-associated cases ($\psi = 0°$) consistently yielded lower FoS values than associated ones ($\psi = \phi$), with the difference increasing with increasing friction angle and slope inclination. This difference reaches over 14% at $\phi = 35°$ and $\alpha = 35°$. Theoretically, ψ governs shear band orientation and thus mobilized resistance, but practical results revealed that for intermediate values ($0° < \psi < \phi$), the FoS converged around $\psi \approx 20°$, independent of ϕ (for $\alpha = 26.5°$). This convergence is due to the ϕ/c-reduction method in PLAXIS, where ϕ is reduced until it equals ψ, after which both are reduced together. This effectively transitions the model to an associated flow. This implementation limits the sensitivity of the FoS to ψ once this threshold is reached. Hence, while ψ governs strength and deformation behavior, numerical settings and boundary conditions heavily influence its effect on model outcome.

- Retaining structure simulations revealed that the dilatancy angle ψ had a pronounced effect on both the failure mechanism and bending moment distribution, due to the highly constrained deformation in this problem. In the non-associated case ($\psi = 0°$), shear bands developed on both the active and passive sides and the structure experienced higher positive bending moments as it absorbed more load from the weaker soil. In contrast, the associated case ($\psi = \phi$) showed localized failure at the top of the passive side where dilation was restricted by the wall, resulting in higher negative bending moments. Intermediate values of ψ ($0° < \psi < \phi$) exhibited non-linear bending moment trends, with peaks linked to shifts in failure mechanism. These results confirm that in problems involving confined and constrained soil, the dilatancy angle governs not only strength but also the form and type of failure, significantly affecting model outcome.

RQ2: "Which level of mesh refinement converges the model outcome of a slope stability and retaining structure problem when using non-associated plasticity in FEM?"

- Slope stability simulations demonstrated that mesh dependence is negligible when using associated plasticity ($\psi = \phi$), with consistent FoS values and stable shear band patterns even with mesh refinement. In contrast, non-associated plasticity ($\psi = 0°$) exhibited strong mesh sensitivity, where the FoS dropped by 8.5% with mesh refinement. The solution only stabilized after a mesh consisting of 8,000 elements,

with 1.4% variation post-convergence. The shear bands also became significantly thinner with finer meshes due to the lack of an internal length scale, theoretically converging toward zero thickness. The required mesh density for convergence was shown to depend primarily on the geometry, not on strength parameters.

- Retaining structure simulations again revealed that associated plasticity ($\psi = \phi$) produced mesh independent results, with stable bending moments and consistent failure mechanisms across mesh densities. In contrast, non-associated plasticity ($\psi = 0°$) showed strong mesh dependence, especially in the positive bending moment, which varied significantly with refinement. The difference in positive and negative bending moment between coarsest and finest mesh in this case reaches approximately 19% and 9% respectively. The positive bending moment stabilizes after a mesh consisting of 11,000 elements, while the negative bending moment shows a large scatter. Shear strain plots highlighted increasingly narrow and intense shear bands near the base of the wall with finer meshes, which results in variations in bending moment in this area. These findings confirm that non-associated models require finer meshes to capture failure mechanisms accurately, and that mesh sensitivity is amplified in problems with constrained deformation.

RQ3: "Under which conditions can equivalent associated plasticity be applied in FEM models?"

- DSS simulations showed that equivalent associated plasticity can accurately reproduce the mobilized shear strength of a non-associated case. However, the equivalent model introduced greater plastic deformation and a different stress path, due to its higher dilatancy angle. Mohr's circle analysis confirmed that while mobilized strength matched, the maximum shear strength and deformation behavior differs. Thus, the method captures strength equivalence, but not deformation behavior, when replicating non-associated materials.

- In slope stability simulations, the equivalent associated model ($\psi = \phi_{EQV}$) provided mesh independent results, but yielded a conservatively low FoS compared to the non-associated case ($\psi = 0°$) on which it was based. This underestimation is due to the Davis approach representing a lower bound strength assumption. To improve alignment, a reduced friction angle ($\phi_{RED} \approx 0.9\,\phi$) was calibrated in an associated model, successfully matching the FoS of the non-associated case while eliminating mesh sensitivity. These results show that with careful calibration, equivalent associated plasticity offers a viable and efficient alternative for slope stability modeling allowing to replicate strength behavior without numerical instability.

- In the retaining structure simulations, the equivalent associated model ($\psi = \phi_{EQV}$) failed to replicate the behavior of the non-associated case due to highly constrained deformation. It significantly overestimated both positive and negative bending moments, caused by (1) underestimated soil strength shifting more load to the structure, and (2) altered failure mechanisms typical of associated flow. Reducing the friction angle ($\phi_{\mathrm{RED}} = 0.9\phi$) helped align the positive bending moment, but the negative moment could not be matched without applying unrealistic parameters. These results indicate that while friction angle reduction may partially correct strength discrepancies, equivalent associated plasticity is not suitable for problems involving strongly constrained deformation, such as retaining structures.

6.2 Recommendations

- Account for dilatancy in confined and constrained problems. The dilatancy angle ψ has a limited effect, apart from the influence on strength, in unconfined problems like slope stability but becomes critical in problems with constrained deformation, such as retaining structures. Engineers should be cautious when ignoring dilation in these contexts, as it can lead to significantly different failure mechanism prediction and model outcome.

- Be aware of factor of safety (FoS) convergence behavior in a PLAXIS stability analysis. When using non-associated plasticity, PLAXIS enforces a transition to associated behavior when ϕ is reduced to match ψ in the ϕ/c-reduction method. This introduces artificial convergence of FoS at intermediate values of ψ, which should be interpreted carefully and not mistaken for true physical behavior. Note that this is typically the case for high dilatancy angles ($\psi > \phi_{mob}$)

- Use non-associated plasticity with mesh sensitivity in mind. Simulations using $\psi \neq \phi$ are mesh dependent. For reliable results, ensure mesh convergence checks are conducted.
- Interpret equivalent plasticity models as bounds. Use the classical Coulomb model ($\psi = \phi$) as an upper bound and the Davis relation for non-dilatant material ($\psi = 0°$) as a lower bound for soil strength. Intermediate friction angle reductions can offer practical mesh independent approximations, but must be calibrated for each problem. This study proved that using $0.9\,\phi$ in a associated manner is promising. However, additional application have to be tested to consider this approximation robust.

References

Bolton, M. D. (1986). The strength and dilatancy of sands. *Géotechnique*, 36(1):65–78.

Brinkgreve, R., Kumarswamy, S., and Swolfs, W. (2016). *Plaxis 2D 2016 User Manual*. Plaxis bv, Delft, Netherlands.

Chen, X., Wang, D., Yu, Y., and Lyu, Y. (2019). A modified davis approach for geotechnical stability analysis involving non-associated soil plasticity. *Géotechnique*, 70:1109–1119.

Davis, E. (1968). Theories of plasticity and failure of soil masses. *Selected Topics*.

de Borst, R. (1987). Computation of post-bifurcation and post-failure behavior of strain-softening solids. *Computers Structures*, 25(2):211–224.

de Borst, R. and Sabet, S. (2019). Mesh bias and shear band inclination in standard and non-standard continuaarchive of applied mechanics. *Archive of Applied Mechanics*, 89(12).

de Borst, R., Sabet, S. A., and Hageman, T. (2022). Non-associated cosserat plasticity. *International Journal of Mechanical Sciences*, 230:107535.

Desrues, J., Chambon, R., Mokni, M., and Mazerolle, F. (1996). Void ratio evolution inside shear bands in triaxial sand specimens studied by computed tomography. *Géotechnique*, 46(3):529–546.

Di Prisco, C. and Pisanò, F. (2011). An exercise on slope stability and perfect elastoplasticity. *Géotechnique*, 61(11):923–934.

Drucker, D. C. (1959). A definition of stable inelastic material. In *Journal of Applied Mechanics 26*.

Houlsby, G. (1991). How the dilatancy of soils affects their behaviour. Technical report, Department of Engineering Science, Oxford University, U.K.

Mühlhaus, H. B. and Vardoulakis, I. (1987). The thickness of shear bands in granular materials. *Géotechnique*, 37(3):271–283.

POVM (2020). Povm eindige-elementenmethode – een publicatie van de pov macrostabiliteit. Technical report, POV Macrostabiliteit, Tiel, The Netherlands. In the context of the Hoogwaterbeschermingsprogramma (HWBP).

Roscoe, K. (1970). The influence of strains in soil mechanics. *Géotechnique*, 20(2):129–170.

Terzaghi, K. and Peck, R. B. (1948). *Soil Mechanics in Engineering Practice*. Wiley, New York, 1st edition.

Teunissen, J. (2007). On double shearing in frictional materials. *International Journal for Numerical and Analytical Methods in Geomechanics*, 31(1):23–51.

Teunissen, J. (2008). Shear band analysis in the biaxial test. *International Journal of Geomechanics*, 8(5):311–321.

Teunissen, J. (2016). Wrijving in sterkteberekeningen. *Geotechniek, jaargang 20 - nummer 3*.

Teunissen, J. (2022). The influence of the intermediate stress on the plane strain strength. *Computers and Geotechnics*, 152:104983.

Tschuchnigg, F., Oberhollenzer, S., and Schweiger, H. (2018). Slope stability analyses considering non-associated plasticity: Application to boundary value problem. *ce/papers*, 2(2-3):809–814.

Tschuchnigg, F., Schweiger, H., and Sloan, S. (2015). Slope stability analysis by means of finite element limit analysis and finite element strength reduction techniques. part ii: Back analyses of a case history. *Computers and Geotechnics*, 70:178–189.

Vaughan, P. R. (1994). Assumption, prediction and reality in geotechnical engineering. *Géotechnique*, 44(4):573–609.

Vermeer, P. and de Borst, R. (1984). *Non-associated plasticity for soils, concrete and rock*. HERON vol. 29, no.3.

Vermeer, P. A. (1990). The orientation of shear bands in biaxial tests. *Géotechnique*, 40(2):223–236.

Zienkiewicz, O. C., Humpheson, C., and Lewis, R. W. (1975). Associated and non-associated visco-plasticity and plasticity in soil mechanics. *Géotechnique*, 25(4):671–689.